Utrecht University

Master's Thesis in Theoretical Physics

Chiral Symmetry Breaking
in Novel Kagome Materials

Supervisor : Dr. Lars Fritz

Author : Riccardo Ciola

Academic Year 2020/2021

Acknowledgements

Contents

Abstract

In the last decades, graphene has been the case study material for many phenomena in different fields of solid state physics. In particular, it has been used to study the electron transport properties of 2D Weyl semimetals, a class of materials characterized by the presence of massless quasi-particle excitations. Recently, a new type of 2D Weyl semimetals, the Kagome system, has been proposed as a better candidate for the realisation of strongly correlated electron fluids. In this thesis, we will test this hypothesis by studying the Coulomb-driven semimetal-insulator phase transition. Specifically, we analyse the effects of the electron-electron interaction both in the weak and strong coupling limit. The former is studied through the renormalization group analysis, the second by numerically solving the self-consistent Schwinger-Dyson equation. Moreover, we discuss the differences between the symmetry breaking process corresponding to the graphene and Kagome phase transition.

Chapter 1

Introduction

The study of 2 dimensional materials is one of the hottest topics in today's theoretical physics. Graphene and other similar systems are applied in a vast range of different fields, from medicine to the development of new materials and technologies. After their first experimental discovery, which occurred in 2004 with the isolation of 2D graphene[1], their use in almost every field of scientific research has started to grow steadily. From a theoretical prospective, they are interesting because of the simplicity that characterizes their structure, and because of the multitude of peculiar phenomena that cannot be observed otherwise. In this thesis, we will focus in particular on the electronic structure of the so-called 2D Weyl semimetals[2]. We will use a combination of classic and new approaches to study the interacting ground state of the well-known graphene model[3][4] and the Kagome lattice[5][6].

1.1   Weyl Semimetals

In solid state physics many of the properties that characterize a material are encoded in its band structure. In particular, we can think of its atoms as fixed points that form a stationary lattice, to which the inner electrons are strongly bounded. Hence, we are interested in the available energy states for the external electrons, which are able to move along this lattice. The initial band structure is derived by assuming that this electrons are non-interacting and using the transnational invariance of the crystal. In this way, we can construct the Bloch Hamiltonian in the momentum space, which describes the single unit cell that composes the lattice. Consequently, the energy levels are defined as the eigenvalues of this Hamiltonian on the Brillouin zone, and they form the band structure of the corresponding material. All the energy levels below the Fermi energy, i.e. the chemical potential at zero temperature, are called valence bands, while those above this energy are the conduction ones.

From this description it is straightforward to distinguish between two limiting cases: metals and insulators. The former are characterized by a gapless spectrum, i.e. the valence and conduction bands live in a continuum and the electrons are almost free to transit from one state to the other. On the contrary, insulators are defined by a finite energy gap between the highest valence band and the lowest conduction band. As a consequence, the Fermi energy lies

within this gap, and a large energy is required to excite an electron between these states.

In addition to these limit cases, it is also possible to observe intermediate configurations. In particular, we will be interested in the so-called semimetals, which are characterized by a gapless spectrum but where the density of states vanishes at the Fermi energy. In general, even though this condition might appear unstable, most semimetals posses different mechanisms that protect their structure. Thus, it is interesting to study under which circumstances, e.g. the electron-electron or the electron-phonon interactions, we can break this picture and lead to a semimetal-insulator or semimetal-metal phase transition.

An interesting subgroup of this category is represented by the Weyl semimetals[2] [3]. These materials are characterized by the presence of Weyl quasiparticle excitations, i.e. massless chiral fermions. Because they are semimetals, the spectrum intersects the Fermi energy surface only in a finite number of points, called the Weyl nodes, at which the density of states vanishes linearly. Consequently, in the vicinity of these points, the electrons behave as massless particles. This implies that at low energies the electrons mimic the physics of relativistic fermions, hence they are able to show some of the peculiar characteristics of quantum electrodynamics (QED). Furthermore, they propagate at a typical velocity v_F, that results much slower than the speed of light. Thus, we expect this relativistic phenomena to occur at a completely different energy scale compared with that of QED. For instance, a famous example of the massless behaviour of the conduction electrons is given by the Klein paradox[3]. It can be shown that the Weyl quasi-particle excitations propagate through a square-well potential according to the same relation that holds for massless, relativistic particles, i.e. preventing any kind of back-scattering along specific directions.

1.1.1   2D Semimetal-Insulator Phase Transition

The Hamiltonian of a generic Weyl semimetal can be effectively expanded at linear order in the vicinity of the Weyl nodes, i.e.

$$H = v_F \mathbf{p} \cdot \boldsymbol{\sigma} \ . \tag{1.1}$$

Here v_F is the electron velocity, $\mathbf{p}$ represents the momentum, and $\boldsymbol{\sigma}$ are the common Pauli matrices. Now the question is how can we open an energy gap at these nodes?

First of all, we have to observe that the large stability of the gapless structure is guaranteed by the material topology[2]. In fact, in any Weyl semimetal we always find an even number of independent nodes. For instance, the graphene lattice that we will analyse in the next chapters present six Dirac points, only two of which are independent. This implies that, in order to produce a gap, we have to act on at least two distinct points of the Brillouin zone, i.e. by means of a perturbation that is non-local in the momentum. It is worth noticing that this represents an interesting difference with the usual behaviour of

other topological materials, e.g. the topological insulators. In these cases, the energy structure is gapped in the bulk and metallic on the edges, thus we need to close the bulk Hamiltonian in order to be able to change the topological invariant of the system, and thus produce a phase transition.

If we now reduce our discussion to the two dimensional materials, the linear Hamiltonian reduces to

$$H = v_F(p_x\sigma_x + p_y\sigma_y) \ . \tag{1.2}$$

Hence the spectrum becomes gapped by introducing a mass term along the excluded dimension, i.e. $\Delta(\mathbf{k})\sigma_z$. We will present explicit examples for this gap function $\Delta(\mathbf{k})$ in the next chapters of the thesis. In any case, it should be clear at this point that this order parameter has to be related to a proper global symmetry of the system. The form of the Hamiltonian (1.2) is a further incentive to study this particular phase transition in the two dimensional case, which can be gapped more easily than its three dimensional counterpart.

1.2 Motivations

The peculiar electronic structure of Weyl semimetals has been used to study numerous phenomena within solid state physics. In particular, we are interested here in the electron transport properties of these materials[7]. In this section we will give a brief justification of the project so as to include it in the more general framework of which it is just a small part.

In general, if we aim to describe the interacting picture of electrons inside a conducting material, we have to deal with at a large number of possible contributions, e.g. electron-electron, electron-phonon and electron-impurities interactions. Consequently, we can define some typical length scales to describe these scattering processes, namely l_{ee}, l and W. The first measures the mean free path for electron-electron collisions, the second is the mean free path with respect to the all the interactions that do not preserve the electron momentum, and lastly W is the sample size. In a typical conductor, the e-e scattering length is much larger than the mean free path l, hence this interaction contributes only marginally to the transport properties. This can be understood by looking at the typical behaviour for different temperature regimes. At low temperatures, the lattice vibrations decrease, thus making the length l longer. However, also l_{ee} grows due to the Fermi statistics that limits the available phase space for e-e collisions. On the contrary, at high temperatures both the electron-phonon and the electron-electron scattering processes increase, thus reducing the length l and l_{ee}. Experimentally, it has been found that there is no metals for which the relation $l_{ee} \ll l$ holds at any temperature scale.

Let assume now that such a material exists, namely such that the e-e interaction gives the dominant contribution in the scattering process. Thus, the conduction electrons would behave as a viscous fluid described by hydrodynamic equations[7]. In fact, within this assumption, the thermal vibrations

and the lattice impurities are not able to destroy the collective response of electrons, as it happens instead in normal materials. This condition would imply numerous peculiar consequences, which could be observed by studying the electron transport properties of the material.

In the last decade it has been argued that Weyl semimetals at low temperature might be a good candidate to observe these peculiar phenomena[7]. In fact, thanks to the vanishing DOS at the Dirac nodes, the long range Coulomb interactions are weakly screened, and thus collective electronic states might be created. In particular, graphene has been object of numerous experiments which studied its transport properties, and other 2D materials have been suggested as possible alternatives.

In this thesis, we will not focus our attention on the electron hydrodynamic regime per se. Instead, we are going to study quantitatively under which conditions an energy gap is opened both in the graphene and Kagome lattice. In fact, the latter has been recently proposed as a valid alternative for the realisation of an electronic fluid[8]. In particular, if compared to graphene, the proposed material is characterized by a stronger Coulomb interaction, i.e. the corresponding coupling parameter is roughly three times larger. On one hand, this might indeed enhanced the Coulomb interaction strength, thus facilitating the realisation of the hydrodynamic regime. At the same time, its stronger interaction might compromise the gapless structure of the Weyl energy bands, thus preventing the formation of collective states. For these reasons, we will study the semimetal-insulator phase transition for these materials under the action of the electron-electron Coulomb interaction alone.

Chapter 2

Renormalization Group Analysis

In this chapter, we will present the electronic structure of pristine monolayer graphene[3][4], which is characterized by the presence of two independent Dirac points. Then, we will study the effects of the electron-electron Coulomb interaction on its energy spectrum, with particular attention to the behaviour in the low energy expansion. We will use the renormalization group theory[9] to determine whether the coupling parameter becomes strong enough to open an energy gap, or if it flows to the weak coupling regime.

2.1 Tight-binding Model

A single sheet of graphene is made out of carbon atoms arranged in hexagonal configurations, as shown in Fig. 2.1. Therefore, it is possible to describe this honeycomb structure as composed by two triangular sublattices, A and B, with lattice vectors

$$\mathbf{a}_1 = \frac{a}{2}\left(3, \sqrt{3}\right) , \qquad \mathbf{a}_2 = \frac{a}{2}\left(3, -\sqrt{3}\right) .$$

Here a represents the carbon-carbon distance, that is of the order of $a \approx 1.42\text{Å}$ for pristine graphene.

In neutral graphene, only one valence electron can move between different carbon atoms, thus generating the entire electronic structure. Throughout the whole discussion, we will consider only hopping between nearest neighbour sites. In fact, including the hopping to the next nearest neighbours contribution would only shift the energy spectrum by a constant factor without acting on the linear expansion around the Dirac points. In other words, the correction due to longer electron hopping is at least of second order, thus irrelevant to the following discussion. The tight-binding Hamiltonian has then the form[3]

$$H = -t \sum_{<i,j>,\sigma} \left(a_{\sigma,i}^\dagger b_{\sigma,j} + b_{\sigma,j}^\dagger a_{\sigma,i}\right) , \tag{2.1}$$

where t is the hopping parameter, $a_{\sigma,i}^\dagger(a_{\sigma,i})$ creates(annihilates) an electron with spin σ on site i on sublattice A, and the sum is taken over the nearest
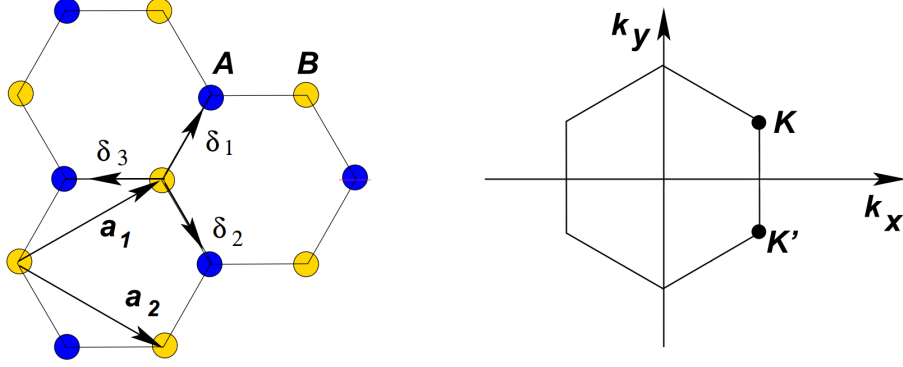
Figure 2.1: (Left) : Lattice structure of graphene. The triangular sublattices, A and B, are described by the lattice unit vectors $\mathbf{a}_1$ and $\mathbf{a}_2$, and they are connected by the nearest neighbour vectors $\boldsymbol{\delta}_i$. (Right) The corresponding Brillouin zone. The two independent Dirac points are located at $\mathbf{K}$ and $\mathbf{K}'$. (adapted from [3])

neighbour sites only.

We can now transform the Hamiltonian to the momentum space by using

$$a_i^\dagger = \frac{1}{\sqrt{N/2}} \sum_{\mathbf{k}} e^{-i\mathbf{k}\cdot\mathbf{r}_i} a^\dagger(\mathbf{k}) \qquad \text{and} \qquad a_i = \frac{1}{\sqrt{N/2}} \sum_{\mathbf{k}} e^{i\mathbf{k}\cdot\mathbf{r}_i} a(\mathbf{k}) \ ,$$

with equivalent expressions for the sublattice B. Since the sum in (2.1) is restricted only to the nearest neighbour sites, the vector positions on the sublattice B can be rewritten as $\mathbf{r}_j = \mathbf{r}_i + \boldsymbol{\delta}$, with $i \in A$, $j \in B$ and

$$\boldsymbol{\delta}_1 = \frac{a}{2}\left(1, \sqrt{3}\right) \qquad \boldsymbol{\delta}_2 = \frac{a}{2}\left(1, -\sqrt{3}\right) \qquad \boldsymbol{\delta}_3 = a\left(-1, 0\right) \ ,$$

as shown in Fig. 2.1. Hence we get

$$H_\sigma = -t \sum_{i \in A} \sum_{\boldsymbol{\delta}} \sum_{\mathbf{k},\mathbf{k}'} \left(\frac{1}{N/2} e^{-i\mathbf{r}_i\cdot(\mathbf{k}-\mathbf{k}')} e^{i\boldsymbol{\delta}\cdot\mathbf{k}'} a_\sigma^\dagger(\mathbf{k}) b_\sigma(\mathbf{k}') + h.c. \right)$$

$$= -t \sum_{\boldsymbol{\delta}} \sum_{\mathbf{k}} \left(e^{i\boldsymbol{\delta}\cdot\mathbf{k}} a_\sigma^\dagger(\mathbf{k}) b_\sigma(\mathbf{k}) + h.c. \right) \ ,$$

where we used that $\sum_{i \in A} e^{i\mathbf{r}_i\cdot(\mathbf{k}-\mathbf{k}')} = \frac{N}{2}\delta(\mathbf{k}-\mathbf{k}')$. Thus, the tight-binding Hamiltonian in the momentum space results

$$H = \sum_{\mathbf{k},\sigma} \bar{\Psi}_\sigma(\mathbf{k}) \begin{pmatrix} 0 & -t\sum_{\boldsymbol{\delta}} e^{i\boldsymbol{\delta}\cdot\mathbf{k}} \\ -t\sum_{\boldsymbol{\delta}} e^{-i\boldsymbol{\delta}\cdot\mathbf{k}} & 0 \end{pmatrix} \Psi_\sigma(\mathbf{k}) \ , \tag{2.2}$$

with $\bar{\Psi}_\sigma(\mathbf{k}) = \begin{pmatrix} a_\sigma^\dagger(\mathbf{k}) & b_\sigma^\dagger(\mathbf{k}) \end{pmatrix}$ and $\Psi_\sigma(\mathbf{k}) = (a_\sigma(\mathbf{k}) \ b_\sigma(\mathbf{k}))^T$. Finally, the eigenvalues of the Bloch Hamiltonian in (2.2) give the energy spectrum of monolayer graphene [3] (see Fig. 2.2), namely

$$E_\pm(\mathbf{k}) = \pm\, t\, \sqrt{3 + 2\cos\left(\sqrt{3}ak_y\right) + 4\cos\left(\frac{\sqrt{3}a}{2}k_y\right)\cos\left(\frac{3a}{2}k_x\right)}$$

The two energy bands are symmetric with respect to the Fermi energy and touch each other at the Dirac points, which are located in the momentum space at

$$\mathbf{K}_D = \left(\frac{2\pi}{3a}, \ \frac{2\pi}{3\sqrt{3}a} \right) \qquad \mathbf{K}'_D = \left(\frac{2\pi}{3a}, \ -\frac{2\pi}{3\sqrt{3}a} \right) \ . \tag{2.3}$$
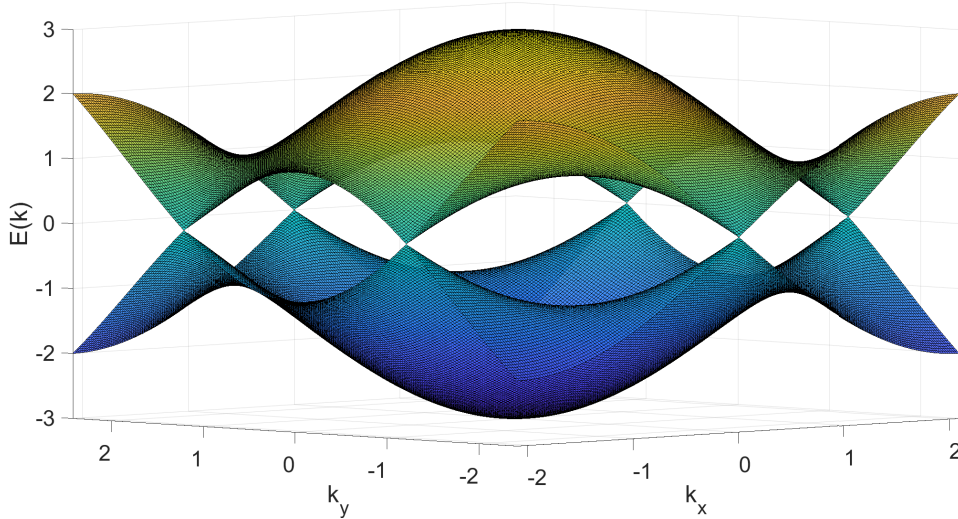
Figure 2.2: Energy spectrum of the non-interacting graphene model (in units of the hopping parameter t).

2.1.1 Linear Expansion

The Bloch Hamiltonian in (2.2) can be expanded at the Dirac points by writing $\mathbf{k} = \mathbf{K}_D + \mathbf{q}$, with $|\mathbf{q}|/|\mathbf{K}_D| \ll 1$, which leads to

$$h(\mathbf{K}_D + \mathbf{q}) = \frac{3}{2}at \begin{pmatrix} 0 & q_x + iq_y \\ q_x - iq_y & 0 \end{pmatrix} = v_F \ \mathbf{q} \cdot \boldsymbol{\sigma} \ , \tag{2.4}$$

where $\boldsymbol{\sigma}$ are the common Pauli matrices. The linear dispersion implies that the electrons at low energy behave as massless, chiral fermions[2][3]. Moreover, the Fermi velocity, defined as $v_F = \frac{3}{2}at$, does not depend on the energy or momentum but it is a property of the material itself. In the case of graphene, the electrons propagate at $v_F \simeq 1 \times 10^6 m/s \sim c/300$.

In the non-interacting case, we observed that the energy spectrum is gapless but with a vanishing density of states (DOS), i.e. graphene behaves as a semimetal. In what follows we will study under which conditions it is possible to open an energy gap spontaneously by means of the electron-electron Coulomb interaction. Thanks to the vanishing DOS, in fact, the long-range Coulomb interactions are weakly screened, which may lead to a renormalization of the band structure close to the Dirac points, i.e. a renormalization of the Fermi velocity.

2.2   Coulomb Interaction

In order to analyse the effects of the Coulomb interaction on the graphene model, we go to the continuum limit in the second quantization language[10][11]. The non-interacting Hamiltonian in the linear regime then becomes[11]

$$H = \int_{|\mathbf{q}|=0}^{\Lambda \sim 1/a} \frac{d\mathbf{q}}{(2\pi)^2} \, \bar{\Psi}(\mathbf{q}) \, v_F \, \mathbf{q} \cdot \boldsymbol{\sigma} \, \Psi(\mathbf{q}) \, , \tag{2.5}$$

where the momentum cut-off is introduced naturally from the lattice constant. In fact, from the energy spectrum (Fig 2.2) and from the definition of the Brillouin zone (Fig. 2.1), we can see that the linear expansion holds in a range that is proportional to the inverse of the lattice constant. We can use this result to write the free action as

$$S_0[\bar{\Psi}, \, \Psi] = \int_0^\beta d\tau \int_{|\mathbf{q}|=0}^{\Lambda \sim 1/a} \frac{d\mathbf{q}}{(2\pi)^2} \, \bar{\Psi}(\mathbf{q}, \tau) \left(\frac{d}{d\tau} + v_F \, \mathbf{q} \cdot \boldsymbol{\sigma} \right) \Psi(\mathbf{q}, \tau) \, , \tag{2.6}$$

which can be Wick rotated by means of the following Fourier transformations

$$\bar{\Psi}(\mathbf{q}, \tau) = \int \frac{d\omega}{2\pi} \, \bar{\Psi}(\mathbf{q}, \omega) e^{i\omega\tau} \qquad \Psi(\mathbf{q}, \tau) = \int \frac{d\omega}{2\pi} \, \Psi(\mathbf{q}, \omega) e^{-i\omega\tau} \, .$$

Then, equation (2.6) at zero temperature becomes

$$S_0[\bar{\Psi}, \, \Psi] = \int_{-\infty}^{\infty} \frac{d\omega}{2\pi} \int_{|\mathbf{q}|=0}^{\Lambda \approx 1/a} \frac{d\mathbf{q}}{(2\pi)^2} \, \bar{\Psi}(\mathbf{q}, \omega) \left(-i\omega \mathbb{1} + v_F \, \mathbf{q} \cdot \boldsymbol{\sigma} \right) \Psi(\mathbf{q}, \omega) \, . \tag{2.7}$$

The action for the Coulomb interaction can be written in the coordinate space as[11]

$$S_{int}[\bar{\Psi}, \, \Psi] = \int d\tau \int d\mathbf{r}_1 \int d\mathbf{r}_2 \, \bar{\Psi}(\mathbf{r}_1, \tau) \bar{\Psi}(\mathbf{r}_2, \tau) V_C(\mathbf{r}_1 - \mathbf{r}_2) \Psi(\mathbf{r}_2, \tau) \Psi(\mathbf{r}_1, \tau) \, . \tag{2.8}$$

It is worth noticing that the interaction term is completely independent of time. This is because, as we discussed in the previous section, the electron velocity is roughly 300 times smaller than the speed of light at which the interaction propagates, i.e. the effects of retardation due to their relative speed are completely irrelevant at this stage. Since graphene is a 2 dimensional model, the Coulomb potential, $V_C(\mathbf{r}) = \frac{e^2}{4\pi\epsilon} \frac{1}{|\mathbf{r}|}$, transforms differently to the momentum space, namely

$$V_C(\mathbf{q}) = \int d\mathbf{r} \frac{e^2}{4\pi\epsilon} \frac{1}{|\mathbf{r}|} e^{-i\mathbf{r} \cdot \mathbf{q}}$$

$$= \frac{e^2}{4\pi\epsilon} \int_0^\infty dr \, r \int_0^{2\pi} d\theta \frac{e^{-irq\cos(\theta)}}{r}$$

$$= \frac{e^2}{4\pi\epsilon} \int_0^\infty \frac{dr'}{|\mathbf{q}|} 2\pi J_0(r')$$

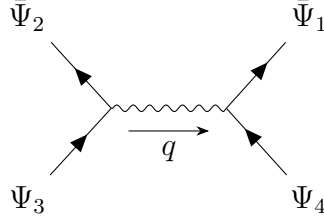$$= \frac{2\pi e^2}{4\pi\epsilon} \frac{1}{|\mathbf{q}|} \, ,$$

Figure 2.3: Diagrammatic representation of the Coulomb interaction. The momentum $\mathbf{q}$ is transferred between the electrons (solid arrows) by means of a photon (wiggly line).

where we defined $r' = rq$, and $J_0(r')$ is a Bessel function of the first kind. In order to transform equation (2.8) we need to perform the following Fourier transformations

$$\bar{\Psi}(\mathbf{r}, \tau) = \int \frac{d\mathbf{q}}{(2\pi)^2} \, \bar{\Psi}(\mathbf{q}, \omega) e^{-i\mathbf{q}\cdot\mathbf{r}+i\omega\tau}$$

$$\Psi(\mathbf{r}, \tau) = \int \frac{d\mathbf{q}}{(2\pi)^2} \, \Psi(\mathbf{q}, \omega) e^{i\mathbf{q}\cdot\mathbf{r}-i\omega\tau}$$

$$V_C(\mathbf{r}) = \int \frac{d\mathbf{q}}{(2\pi)^2} \, V_C(\mathbf{q}) e^{i\mathbf{q}\cdot\mathbf{r}} \ .$$

Combining all these expressions together, we get the general formula for the Coulomb action in 2 dimensions, i.e.

$$S_{int}[\bar{\Psi}, \ \Psi] = \prod_{n=1}^{4} \int_{-\infty}^{\infty} \frac{d\omega_n}{2\pi} \int_{|\mathbf{p}_n|=0}^{\Lambda \sim 1/a} \frac{d\mathbf{p}_n}{(2\pi)^2} \int_{|\mathbf{q}|=0}^{\Lambda \sim 1/a} \frac{d\mathbf{q}}{(2\pi)^2}$$

$$\bar{\Psi}(\mathbf{p}_1, \omega_1) \bar{\Psi}(\mathbf{p}_2, \omega_2) \frac{2\pi e^2}{4\pi\epsilon} \frac{1}{|\mathbf{q}|} \ \Psi(\mathbf{p}_3, \omega_3) \Psi(\mathbf{p}_4, \omega_4)$$

$$(2\pi)^2 \delta (\mathbf{p}_1 - \mathbf{p}_4 - \mathbf{q}) (2\pi)^2 \delta (\mathbf{p}_2 - \mathbf{p}_3 + \mathbf{q}) (2\pi) \delta (\omega_1 + \omega_2 - \omega_3 - \omega_4) \ .$$

$$(2.9)$$

In this expression, the first two delta functions represent the conservation of the momentum, while the third one preserves the energy. The physical meaning can be better understood by looking at its diagrammatic representation, which is shown in Fig. 2.3. From this, it is easier to comprehend why also the integral over the Coulomb potential is restricted to Λ, i.e. because the momentum is completely transferred from one electron to the other, which are both limited in the low energy approximation.

2.3 Renormalization Group

The renormalization group[9][10] (RG) is a set of symmetry operations, i.e. transformations that leave the physics invariant, which rescale the characteristic length scales of the problem. Originally, it has been introduced to deal with the ultraviolet divergences that appear in high-energy theories, such as

QED. In these cases, a cut-off, called Λ, is needed in order to prevent the physical quantities from diverging, which thus means confining the problem to the relevant energy scale we are looking for. The idea of the RG is to find a set of Λ-dependent coupling functions, $\alpha(\Lambda)$, such that the relevant physical quantities result cut-off independent. This can be done for any renormalizable field theory, for which exists a finite set of parameters that satisfy this condition. Finding this group corresponds to work out how the set of coupling functions behave under a change of the cut-off, which is usually expressed through the β-function

$$\beta(\alpha) = \frac{d\alpha}{db} \ , \tag{2.10}$$

where the cut-off is $\Lambda = \Lambda(b)$. This method allows you to study how to modify the coupling parameters while sending the cut-off to infinity, which is where the field theory has physical meaning, meanwhile the relevant physical quantities are invariant under these transformations.

In low-energy physics, however, this method acquires a completely new point of view[9]. As we discussed in the previous sections, the cut-off Λ is no longer an artefact of the theory, but it rather sets an upper limit to the energy scale of interest. Moreover, the cut-off is often provided by some natural quantity of the system, such as the inverse lattice spacing, and it does not hide any kind of ultraviolet divergences. In this context, the RG approach consists of three distinct steps.

Step 1 : mode elimination
Usually, when dealing with condensed matter systems, we are interested in studying the divergence of some correlation length at the critical point. However, the relevant correlations are by definition those of modes that lie within a ball of size Λ/b, with $b > 1$. This implies that we can separate the fields into *slow* and *fast* modes, i.e.

$$\phi_< = \phi(k) \quad for \quad 0 < k < \Lambda/b \quad (slow \ modes)$$
$$\tag{2.11}$$
$$\phi_> = \phi(k) \quad for \quad \Lambda/b < k < \Lambda \quad (fast \ modes) \ .$$

The first step consists of rewriting the theory as an effective theory for the *slow* modes only, which can be done by expressing the action as

$$S[\phi_<, \ \phi_>] = S_0[\phi_<] + S_0[\phi_>] + S_{int}[\phi_<, \ \phi_>] \ . \tag{2.12}$$

It is important to notice that the non-interacting part automatically separates into *slow* and *fast* contributions since it is a quadratic function of the fields, hence any term that contains both modes integrates to zero. Then, we use equation (2.12) to write the effective partition function as following

$$Z = \int [d\phi_<] \, [d\phi_>] \, e^{S_0[\phi_<]} e^{S_0[\phi_>]} e^{S_{int}[\phi_<, \ \phi_>]}$$

$$= \int [d\phi_<] \, e^{S_0[\phi_<]} \int [d\phi_>] \, e^{S_0[\phi_>]} e^{S_{int}[\phi_<, \ \phi_>]} \tag{2.13}$$

$$= \int [d\phi_<] \, e^{S'[\phi_<]} \ ,$$

which defines the *slow* modes effective action $S'[\phi_<]$. This partition function provides a good description of the *slow* modes physics, integrating out of the picture the short wavelengths contribution.

Step 2 : rescaling momenta
In principle, the next step would be to compute the β-function defined by (2.10), i.e. compare the coupling functions that appear in the original action $S[\phi]$ with the ones from the rescaled $S'[\phi_<]$. However, this cannot be done directly since they are defined on different domains, i.e. $\alpha(\Lambda)$ has no match in the rescaled theory. To overcome this issue, we define new momenta after the mode elimination through $k' \doteq bk$. In this way the *slow* modes still run up to the original cut-off Λ again.

Step 3 : rescaling fields
A direct comparison of the actions would still not be free from redundancies lacking of physical meaning. In fact, at this point the fields that appear in the actions are not physically equivalent, thus we need to find some other quantity that allows us to relate them. A possible solution is to identify one of the coupling constant as an invariant under the renormalization group action, and rescale the new fields accordingly. In other words, once we assume one of the parameter is invariant, we transform the fields in such a way that it results explicit under the RG.

Once all the three steps are accomplished, we are able to compare different actions defined on the same space. In order to do this, we introduce the concept of *flow diagram*, i.e. how the coupling constants change under the action of the RG. In other words, we can picture the two actions, $S[\phi]$ and $S'[\phi']$, as distinct points in a coupling constant space, and the RG tells you how these two points are related, i.e. how the initial action *flows* to the transformed one. This procedure allows us to find fixed points of the group action, namely points of the flow diagram that do not transform under the RG action. This means that the relevant physical quantities of these theories, i.e. the correlation lengths, are either zero or infinite. While the first case represents a trivial situation, the latter indicates we approached a critical point for the model in exam.

In the next paragraphs we will apply this method to the linear, tight-binding model of graphene with interacting electrons[3][4]. We will see how to identify the proper coupling constant for the theory, and analyse the effects of the Coulomb interaction using the flow diagram concept.

2.3.1   First Oder Approximation

To study the renormalization group action, we start with the zero temperature partition function, namely

$$Z = \int d\left[\bar{\Psi}\right] d\left[\Psi\right] e^{-S_0\left[\bar{\Psi},\,\Psi\right]} e^{-S_{int}\left[\bar{\Psi},\,\Psi\right]} \,, \tag{2.14}$$

where $S_0\left[\bar{\Psi},\ \Psi\right]$ and $S_{int}\left[\bar{\Psi},\ \Psi\right]$ are given by equation (2.7) and (2.9) respectively. Hence, we apply the first step, i.e. the mode elimination, by splitting the fields into slow and fast modes. The effective action defined in equation (2.13) thus becomes

$$
\begin{aligned}
e^{-S'\left[\bar{\Psi}_<,\ \Psi_<\right]} &= e^{-S_0\left[\bar{\Psi}_<,\ \Psi_<\right]} \int d\left[\bar{\Psi}_>\right] d\left[\Psi_>\right] e^{-S_0\left[\bar{\Psi}_>,\ \Psi_>\right]} e^{-S_{int}\left[\bar{\Psi}_>,\ \Psi_>,\ \bar{\Psi}_<,\ \Psi_<\right]} \\[2mm]
&= e^{-S_0\left[\bar{\Psi}_<,\ \Psi_<\right]} Z_0^> \left\langle e^{-S_{int}\left[\bar{\Psi}_>,\ \Psi_>,\ \bar{\Psi}_<,\ \Psi_<\right]} \right\rangle_> \\[2mm]
&= e^{-S_0\left[\bar{\Psi}_<,\ \Psi_<\right]} Z_0^> \left(e^{-\langle S_{int}\rangle_> + \frac{1}{2}\left(\langle S_{int}^2\rangle_> - \langle S_{int}\rangle_>^2\right) + \mathcal{O}(S_{int}^3)} \right) .
\end{aligned}
$$
(2.15)

Here $\langle\ \cdot\ \rangle_>$ represents the non-interacting average over the fast modes, and $Z_0^>$ is the free partition function in the short wavelength regime, which is needed to normalize the interacting average (*see Appendix A*).

The first order approximation consists of considering only the first term in the above expansion, i.e. $e^{-\langle S_{int}\rangle_>}$. According to equation (A.1), this can be written in the following expression

$$
\langle S_{int}\rangle_> = \left\langle S_{int}\left[\bar{\Psi}_<,\ \Psi_<\right]\right\rangle_{>,1} + \left\langle S_{int}\left[\bar{\Psi}_>,\ \Psi_>,\ \bar{\Psi}_<,\ \Psi_<\right]\right\rangle_{>,2} ,
$$
(2.16)

where the right-hand terms are given by equation (A.2) and (A.5) respectively. The next step of the RG analysis is to rescale the momenta such that the original cut-off is restored, namely

$$
\mathbf{p}' = b\,\mathbf{p}
$$
$$
\omega' = b\,\omega .
$$
(2.17)

Finally, we need to transform the fields according to the third step of the RG method. In this case, the idea is to formally rewrite the partition function (2.14), where now $\langle S_{int}\rangle_{>,1}$ provides for the whole interacting term, while $\langle S_{int}\rangle_{>,2}$ modifies the free contribution. This can be achieved by using

$$
\bar{\Psi}'\left(\mathbf{p}',\ \omega'\right) = b^{-2}\,\bar{\Psi}_<\left(\mathbf{p},\ \omega\right)
$$
$$
\Psi'\left(\mathbf{p}',\ \omega'\right) = b^{-2}\,\Psi_<\left(\mathbf{p},\ \omega\right) ,
$$
(2.18)

which formally transforms $\langle S_{int}\rangle_{>,1}$ into equation (2.9) with the new, primed fields.

The non-interacting contribution is now composed by the original action plus the one-loop correction due to $\langle S_{int}\rangle_{>,2}$. Finally, we have to analyse the effect of this term as a function of the cut-off Λ in the low energy limit. Hence, we need to study the self energy term given by equation (A.6), namely

$$
\Sigma^{(1)}\left(\mathbf{q}\right) = \int_{-\infty}^{\infty} \frac{d\omega}{2\pi} \int_{\Lambda/b}^{\Lambda} \frac{d\mathbf{p}}{(2\pi)^2} \frac{1}{|\mathbf{p}-\mathbf{q}|} G_{0,>}\left(\mathbf{p},\omega\right) .
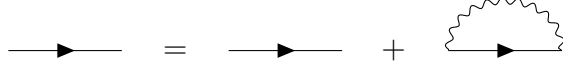$$
(2.19)

Figure 2.4: Diagrammatic representation of the first order Hartree-Fock approximation[10].

This is the usual one-loop correction that comes from the first order perturbation theory (see Fig. 2.4). The non-interacting Green's function can be obtained by its inverse, which is defined implicitly in equation (2.7), leading to[4]

$$G_0\left(\mathbf{p}, \omega\right) = \left(-i\omega\mathbb{1} + v_F\ \mathbf{p}\cdot\boldsymbol{\sigma}\right)^{-1}$$

$$= \frac{i\omega\mathbb{1} + v_F\ \mathbf{p}\cdot\boldsymbol{\sigma}}{\omega^2 + v_F^2|\mathbf{p}|^2}\ . \tag{2.20}$$

Inserting this equation into the self energy expression, and noticing that the terms that are odd in frequency becomes zero when integrated, we get

$$\Sigma^{(1)}\left(\mathbf{q}\right) = \int_{-\infty}^{\infty} \frac{d\omega}{2\pi} \int_{\Lambda/b}^{\Lambda} \frac{d\mathbf{p}}{(2\pi)^2} \frac{1}{|\mathbf{p}-\mathbf{q}|} \frac{v_F\ \mathbf{p}\cdot\boldsymbol{\sigma}}{\omega^2 + v_F^2|\mathbf{p}|^2}\ .$$

The goal of this term is to renormalize the Fermi velocity that appears in the non-interacting action (2.7). Hence, we can rewrite the above expression in such a way that the momentum dependency goes explicitly like $\sim \mathbf{q}\cdot\boldsymbol{\sigma}$. We can achieve this by defining a new function $\Sigma^{(1)}\left(\mathbf{q}\right) = \bar{\Sigma}\left(\mathbf{q}\right)\mathbf{q}\cdot\boldsymbol{\sigma}$, which then satisfies

$$Tr\left(\mathbf{q}\cdot\boldsymbol{\sigma}\Sigma^{(1)}\left(\mathbf{q}\right)\right) = Tr\left(\mathbf{q}\cdot\boldsymbol{\sigma}\ \bar{\Sigma}\left(\mathbf{q}\right)\ \mathbf{q}\cdot\boldsymbol{\sigma}\right)$$

$$= |\mathbf{q}|^2\ \bar{\Sigma}\left(\mathbf{q}\right)\ Tr\left(\mathbb{1}\right)\ . \tag{2.21}$$

In the end we get

$$\bar{\Sigma}\left(\mathbf{q}\right) = \frac{1}{2|\mathbf{q}|^2}Tr\left(\mathbf{q}\cdot\boldsymbol{\sigma}\Sigma^{(1)}\left(\mathbf{q}\right)\right)$$

$$= \frac{1}{2|\mathbf{q}|^2} \int_{-\infty}^{\infty} \frac{d\omega}{2\pi} \int_{\Lambda/b}^{\Lambda} \frac{d\mathbf{p}}{(2\pi)^2} \frac{1}{|\mathbf{p}-\mathbf{q}|} \frac{Tr\left(\left(\mathbf{q}\cdot\boldsymbol{\sigma}\right)\left(v_F\mathbf{p}\cdot\boldsymbol{\sigma}\right)\right)}{\omega^2 + v_F^2|\mathbf{p}|^2} \tag{2.22}$$

$$= \frac{1}{2|\mathbf{q}|^2} \int_{\Lambda/b}^{\Lambda} \frac{dp\ p}{(2\pi)^2} \int_0^{\pi} d\theta \frac{|\mathbf{q}|\cos(\theta)}{\sqrt{p^2 + |\mathbf{q}|^2 - 2p|\mathbf{q}|\cos(\theta)}}\ ,$$

where we used that

$$Tr\left(\left(\mathbf{q}\cdot\boldsymbol{\sigma}\right)\left(v_F\mathbf{p}\cdot\boldsymbol{\sigma}\right)\right) = v_F Tr\left(\left(\mathbf{q}\cdot\mathbf{p}\right)\mathbb{1} + i\left(\mathbf{q}\times\mathbf{p}\right)\cdot\boldsymbol{\sigma}\right)$$

$$= 2v_F\ \mathbf{q}\cdot\mathbf{p}\ , \tag{2.23}$$

and

$$\int_{-\infty}^{\infty} \frac{d\omega}{2\pi} \frac{1}{\omega^2 + v_F^2 p^2} = \frac{1}{2v_F p}\ .$$

To integrate equation (2.22) we notice that, while the integrated momenta $\mathbf{p}$ runs from Λ/b to Λ, the variable $\mathbf{q}$ is restricted to the low energy limit. This implies that we can expand the denominator in the limit $|\mathbf{q}|/|\mathbf{p}| \ll 1$, i.e.

$$\bar{\Sigma}\left(\mathbf{q}\right) = \frac{1}{2|\mathbf{q}|} \int_{\Lambda/b}^{\Lambda} \frac{dp}{(2\pi)^2} \int_0^\pi d\theta \; p \; \cos(\theta) \left(1 + \frac{|\mathbf{q}|}{p} \cos(\theta) + \mathcal{O}\left(\frac{|\mathbf{q}|^2}{p^2}\right)\right)$$

$$\simeq \frac{1}{16\pi}\left(\log\left(\Lambda\right) - \log\left(\Lambda/b\right)\right) \; . \tag{2.24}$$

Finally, we can substitute the self energy expression into the equation (A.5) to obtain the correction to the non-interacting action. However, it is important to notice that the original action is proportional to the Fermi velocity alone, while the term we just computed is still related to the Coulomb strength $\frac{e^2}{4\pi\epsilon}$, as shown by equation (2.9). In fact, we are studying here how the electronic interaction acts on the kinetic part of the Hamiltonian, which is expressed by the tight-binding model. This problem is solved by introducing a coupling term between these two contributions, namely

$$\alpha = \frac{e^2}{4\pi\epsilon}\frac{1}{v_F} \; . \tag{2.25}$$

First of all, we see that this term allows us to express the relevant correction, i.e. $\langle S_{int}\rangle_2$, as a function of the Fermi velocity. In fact, combining $\langle S_{int}\rangle_2$ with $S_0\left[\bar{\Psi}_<, \; \Psi_<\right]$ according to (2.15), we get[4]

$$S_0 = \int_{-\infty}^{\infty} \frac{d\omega}{2\pi} \int_{|\mathbf{p}|=0}^{\Lambda/b} \frac{d\mathbf{p}}{(2\pi)^2} \; \bar{\Psi}_<\left(\mathbf{p},\omega\right)\left[\left(1 + \frac{\alpha}{4}\left(\log\left(\Lambda\right) - \log\left(\frac{\Lambda}{b}\right)\right)\right) v_F \; \mathbf{p}\cdot\boldsymbol{\sigma}\right]\Psi_<\left(\mathbf{p},\omega\right) \; . \tag{2.26}$$

Before we analyse what this expression means in terms of the renormalization group theory, it is important to give a physical interpretation to the coupling constant (2.25). We see from the definition that it represents the ratio between the electrostatic and the kinetic energy, that is proportional to v_F. In other words, we expect the linear picture, i.e. the massless character of the electrons, to break down when α becomes large, namely when the Coulomb interaction dominates. On the contrary, if the coupling parameter *flows* to small values, the gapless structure is preserved.

We observed that the slow modes contribution to the interaction, i.e. $\langle S_{int}\rangle_1$, transforms into the original Coulomb action under the RG process. Similarly, equation (2.26) has to become the original non-interacting action now that we included the one-loop correction through the self energy diagram. This is obtained by introducing a scale dependency in the Fermi velocity, and writing the expression (2.26) as the non-interacting, slow modes contribution, i.e.[4]

$$v_F\left(\frac{\Lambda}{b}\right) = \left[1 + \frac{\alpha}{4}\left(\log\left(\Lambda\right) - \log\left(\frac{\Lambda}{b}\right)\right)\right] v_F(\Lambda) \; . \tag{2.27}$$

We are considering here the low energy limit, which corresponds to taking a large value of the renormalization parameter b such that the momentum

shell becomes $\Lambda/b \ll \Lambda$. If we study the above relation as a function of the renormalized cut-off $k = \Lambda/b$, we get

$$v_F(k) = \left[1 + \frac{\alpha}{4} \log\left(\frac{\Lambda}{k}\right)\right] v_F(\Lambda) \ .$$

Thus, introducing the RG scale $l = log(\Lambda/k)$ and using the definition of the coupling parameter (2.25), we end up with

$$\frac{dv_F(k)}{dl} = \frac{v_F(\Lambda)\alpha}{4} = \frac{e^2}{16\pi\epsilon} \ . \tag{2.28}$$

If we now use that the electronic charge does not flow, i.e. it is invariant under the RG transformations, we find

$$\frac{de^2}{dl} = 0 = \alpha\frac{dv_F}{dl} + v_F\frac{d\alpha}{dl} \ , \tag{2.29}$$

which, together with the first relation of (2.28), becomes

$$\frac{d\alpha}{dl} = -\frac{\alpha^2}{4} \ . \tag{2.30}$$

This is the most important result of the renormalization group method. In fact, integrating (2.30) in the low energy limit, we obtain

$$\alpha(k) \sim \frac{4}{\log(\Lambda/k)} \quad , \quad k \to 0 \ , \tag{2.31}$$

which means the coupling parameter flows to the weak coupling regime. In the language of the RG theory, this means that $\alpha = 0$ is a fixed point towards which it flows logarithmically, i.e. the Coulomb interaction is irrelevant. Moreover, since they are related through the definition (2.25), and the electronic charge is not renormalized, this is equivalent to a logarithmically divergent Fermi velocity. In other words, at the first order analysis the Coulomb interaction flows to the weak coupling regime. This means the energy spectrum remains gapless at the Dirac points, and thus the electrons are still free and massless.

2.3.2 Random Phase Approximation

In the last section, we presented the first order approximation with the bare Coulomb interaction. In principle, this picture can be improved by including the contribution from all the relevant loop diagrams to the interacting term. However, this problem is generally not traceable due to the infinite number of different kind of diagrams that participate to the process. Hence, the idea is to consider the infinite order expansion, necessary to preserve the self-consistency of the expression, in which only the most significant type of diagram is included[12].

In order to find this diagram, we observe that the fermion flavour of graphene is $N = 4$, since we have 2 independent Dirac points and 2 independent spin components. Thus, in the limit of large N, the only relevant contribution is
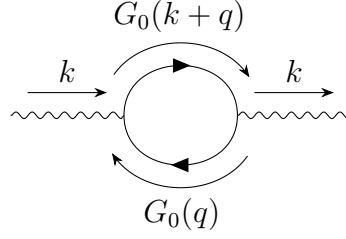
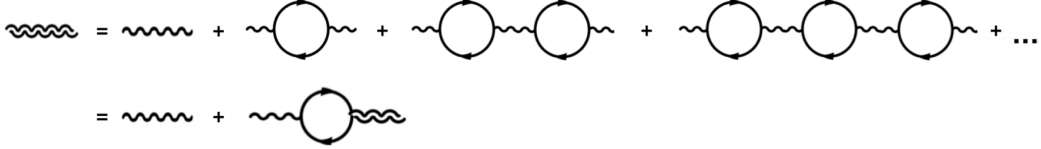Figure 2.5: Diagrammatic representation of the polarization function.

Figure 2.6: Diagrammatic representation of the RPA potential.

given by the bubble diagram shown in Fig. 2.5. In fact, this is the only term that is proportional to the fermion flavour, hence the n-th order expansion will be proportional to N^n. It is straightforward to observe that, even in the case of $N = 4$, the contribution from any other diagram type is dominated by the loop one.

Polarization Function
This approximation is called the random phase approximation (RPA), and can be solved exactly. In fact, we can express the infinite order expansion through the self-consistent equation shown in Fig. 2.6. The polarization function, i.e. the bubble diagram in Fig. 2.5, is then defined as

$$\Pi\left(\mathbf{k}, \omega\right) = N \int \frac{d\nu}{2\pi} \frac{d\mathbf{q}}{(2\pi)^2} \, Tr\left(G_0\left(\mathbf{k} + \mathbf{q}, \omega + \nu\right) G_0\left(\mathbf{q}, \nu\right)\right) \ . \tag{2.32}$$

Hence, using the formula (2.20) for the non-interacting Green's function and the expression (2.23) to work out the trace, we get

$$\Pi\left(\mathbf{k}, \omega\right) = N \int \frac{d\nu}{2\pi} \frac{d\mathbf{q}}{(2\pi)^2} \, Tr\left(\frac{i\left(\omega + \nu\right)\mathbb{1} + v_F\left(\mathbf{k} + \mathbf{q}\right) \cdot \boldsymbol{\sigma}}{\left(\omega + \nu\right)^2 + v_F^2|\mathbf{k} + \mathbf{q}|^2} \, \frac{i\nu\mathbb{1} + v_F\,\mathbf{q} \cdot \boldsymbol{\sigma}}{\nu^2 + v_F^2|\mathbf{q}|^2}\right)$$

$$= N \int \frac{d\nu}{2\pi} \frac{d\mathbf{q}}{(2\pi)^2} \left(\frac{-2\nu\left(\omega + \nu\right) + 2v_F^2\left(\mathbf{k} + \mathbf{q}\right) \cdot \mathbf{q}}{\left[\left(\omega + \nu\right)^2 + v_F^2|\mathbf{k} + \mathbf{q}|^2\right]\left[\nu^2 + v_F^2|\mathbf{q}|^2\right]}\right) \ . \tag{2.33}$$

In order to solve this equation analytically, we rewrite the denominator's product using the Feynman's trick, i.e.

$$\frac{1}{AB} = \int_0^1 dx \, \frac{1}{(xA + (1-x)B)^2} \ . \tag{2.34}$$

In this way, we can find a coordinate transformation that makes the denominator an even function of both frequency and momentum. In particular, introducing the integral (2.34) and then performing the following transformation

$$\begin{aligned}
\nu &\rightarrow \nu - x\omega \\
\mathbf{q} &\rightarrow \mathbf{q} - x\mathbf{k} \;,
\end{aligned}$$

(2.35)

we obtain

$$\Pi\left(\mathbf{k}, \omega\right) = -2N \int \frac{d\nu}{2\pi} \frac{d\mathbf{q}}{(2\pi)^2} \int_0^1 dx \; \frac{(\nu - x\omega)(\nu - x\omega + \omega) - v_F^2 \left(\mathbf{q} - x\mathbf{k} + \mathbf{k}\right) \cdot \left(\mathbf{q} - x\mathbf{k}\right)}{\left[\nu^2 + v_F^2 |\mathbf{q}|^2 + x(1-x)\left(\omega^2 + v_F^2 |\mathbf{k}|^2\right)\right]^2}$$

$$= -2N \int \frac{d\nu}{2\pi} \frac{d\mathbf{q}}{(2\pi)^2} \int_0^1 dx \; \frac{\nu^2 - v_F^2 |\mathbf{q}|^2 - x(1-x)\left(\omega^2 - v_F^2 |\mathbf{k}|^2\right)}{\left[\nu^2 - v_F^2 |\mathbf{q}|^2 + x(1-x)\left(\omega^2 + v_F^2 |\mathbf{k}|^2\right)\right]^2} \;.$$

(2.36)

In the last line we dropped all the terms that were odd either in $\mathbf{q}$ or ν. At this point we can integrate the frequency using the residue theorem and transform the momentum in the polar coordinates. Solving all the remaining integrals analytically, we end up with the following expression for the polarization function[4][12]

$$\Pi\left(\mathbf{k}, \omega\right) = -\frac{N}{16} \frac{|\mathbf{k}|^2}{\sqrt{\omega^2 + v_F^2 |\mathbf{k}|^2}} \;.$$

(2.37)

The interaction term with the random phase approximation is deducted by the diagrammatic representation in Fig. 2.6, namely

$$V^{RPA}\left(\mathbf{k}, \omega\right) = V_C(\mathbf{k}) + V_C(\mathbf{k})\Pi\left(\mathbf{k}, \omega\right) V^{RPA}\left(\mathbf{k}, \omega\right)$$

$$= \frac{1}{V_C^{-1}(\mathbf{k}) - \Pi\left(\mathbf{k}, \omega\right)}$$

$$= \frac{1}{\frac{4\pi\epsilon|\mathbf{k}|}{2\pi e^2} + \frac{N}{16} \frac{|\mathbf{k}|^2}{\sqrt{\omega^2 + v_F^2 |\mathbf{k}|^2}}} \;.$$

(2.38)

It is worth noticing that in the limit of large fermion flavour, i.e. large N, this expression becomes exact. In what follows we will derive the RG equations in this limit, which is a good approximation of the graphene case.

Self Energy

The next step towards the renormalization of the Fermi velocity consists of calculating the self energy[10]. In analogy to what we did in the previous section, we define this function as

$$\Sigma^{RPA}(\mathbf{k}, \omega) = -\int_{\Lambda/b}^{\Lambda} \frac{d\mathbf{p}}{(2\pi)^2} \frac{d\nu}{2\pi} G_0\left(\mathbf{k} + \mathbf{p}, \omega + \nu\right) V^{RPA}\left(\mathbf{p}, \nu\right) \;,$$

(2.39)

where now the bare Coulomb interaction has been replaced by $V^{RPA}(\mathbf{p}, \nu)$. We recall from the first order derivation that the integration variables belong to the outermost shell, while $(\mathbf{k}, \omega)$ are defined on the renormalized domain. Hence, we can expand the Green's function up to the first order, i.e.

$$G_0\left(\mathbf{k} + \mathbf{p}, \omega + \nu\right) \simeq G_0\left(\mathbf{p}, \nu\right) + \omega \frac{\partial G_0\left(\mathbf{p}, \nu\right)}{\partial \nu} + \sum_{i=x,y} k_i \frac{\partial G_0\left(\mathbf{p}, \nu\right)}{\partial p_i} \;.$$

(2.40)

Furthermore, since $V^{RPA}(\mathbf{p}, \nu)$ is even in all its variables, we drop out all the terms in (2.40) that result odd in any of those, obtaining

$$
\Sigma^{RPA}(\mathbf{k}, \omega) = -\int_{\Lambda/b}^{\Lambda} \frac{d\mathbf{p}}{(2\pi)^2} \frac{d\nu}{2\pi} \left[\omega \left(\frac{i\mathbb{1}}{\nu^2 + v_F^2 |\mathbf{p}|^2} - \frac{2i\nu^2 \mathbb{1}}{(\nu^2 + v_F^2 |\mathbf{p}|^2)^2} \right) \right.
$$

$$
\left. + \sum_{i=x,y} k_i \left(\frac{v_F \sigma_i}{\nu^2 + v_F^2 |\mathbf{p}|^2} - \frac{2 v_F^3 p_i \mathbf{p} \cdot \boldsymbol{\sigma}}{(\nu^2 + v_F^2 |\mathbf{p}|^2)^2} \right) \right] V^{RPA}(\mathbf{p}, \nu)
$$

$$
= -\int_{\Lambda/b}^{\Lambda} \frac{d\mathbf{p}}{(2\pi)^2} \frac{d\nu}{2\pi} \left[i\omega \left(\frac{\nu^2 + v_F^2 |\mathbf{p}|^2 - 2\nu^2}{(\nu^2 + v_F^2 |\mathbf{p}|^2)^2} \right) \mathbb{1} \right.
$$

$$
\left. + \left(\frac{v_F \mathbf{k} \cdot \boldsymbol{\sigma}}{\nu^2 + v_F^2 |\mathbf{p}|^2} - \frac{2 v_F^3 \left(k_x \sigma_x p_x^2 + k_y \sigma_y p_y^2 \right)}{(\nu^2 + v_F^2 |\mathbf{p}|^2)^2} \right) \right] V^{RPA}(\mathbf{p}, \nu) \ .
$$

$$(2.41)$$

This integral can be easily expressed in terms of a three-vector that puts together frequency and momentum, namely $\vec{q} = (\nu, \ v_F \mathbf{p})$. Moreover, using this variable the interaction term (2.38) becomes

$$
V^{RPA}(\mathbf{p}, \nu) = \frac{16 v_F^2 \lambda/N}{|\vec{q}| \sin\theta \, (1 + \lambda \sin\theta)} \quad \text{with} \quad \lambda = \frac{\pi}{8} N\alpha \ . \tag{2.42}
$$

This new parameter measures the importance of the loop diagram contribution with respect to the bare Coulomb interaction. Besides, we can use it to describe the coupling strength between the free theory and the interaction term, namely with $\lambda \gg 1$ corresponding to the large fermion flavour limit and $\lambda \ll 1$ to the weak coupling. Hence, the self energy function becomes [4]

$$
\Sigma^{RPA}(\mathbf{k}, \omega) = -\int_{\Lambda/b}^{\Lambda} \frac{d\vec{q}}{v_F^2 (2\pi)^3} \left[\frac{-i\omega}{|\vec{q}|^2} \left(\cos^2\theta - \sin^2\theta \right) \mathbb{1} + v_F \frac{\mathbf{k} \cdot \boldsymbol{\sigma} \cos^2\theta}{|\vec{q}|^2} \right] V^{RPA}(\vec{q})
$$

$$
= -\int_{\Lambda/b}^{\Lambda} \int_0^{\pi} \int_0^{2\pi} \frac{dq\,d\theta\,d\phi \ q^2 \sin\theta}{v_F^2 (2\pi)^3} \left[\frac{-i\omega}{q^2} \left(\cos^2\theta - \sin^2\theta \right) \mathbb{1} \right.
$$

$$
\left. + v_F \frac{\mathbf{k} \cdot \boldsymbol{\sigma} \cos^2\theta}{q^2} \right] \frac{16 v_F^2 \lambda/N}{q \ \sin\theta \, (1 + \lambda \sin\theta)}
$$

$$
= -\frac{8}{N\pi^2} \left[\log(\Lambda) - \log\left(\frac{\Lambda}{b} \right) \right] \left(-i\omega F_{0,\lambda} \mathbb{1} + v_F \mathbf{k} \cdot \boldsymbol{\sigma} F_{1,\lambda} \right) \ ,
$$

$$(2.43)$$

where we used the integral formulas

$$
F_{0,\lambda} = \frac{\lambda}{2} \int_0^{\pi} d\theta \frac{\cos^2\theta - \sin^2\theta}{1 + \lambda \sin\theta} = \begin{cases} \frac{\pi}{\lambda} - 2 - \frac{2-\lambda^2}{\lambda\sqrt{1-\lambda^2}} \arccos\lambda & \lambda < 1 \\ \frac{\pi}{\lambda} - 2 + \frac{\lambda^2-2}{\lambda\sqrt{\lambda-1}} log\left(\lambda + \sqrt{\lambda^2-1}\right) & \lambda > 1 \end{cases}
$$

$$(2.44)$$

$$F_{1,\lambda} = \frac{\lambda}{2} \int_0^\pi d\theta \frac{\cos^2 \theta}{1 + \lambda \sin \theta} = \begin{cases} \frac{\pi}{2\lambda} - 1 - \frac{\sqrt{1-\lambda^2}}{\lambda} \arccos \lambda & \lambda < 1 \\ \frac{\pi}{2\lambda} - 1 + \frac{\sqrt{\lambda^2-1}}{\lambda} log\left(\lambda + \sqrt{\lambda^2 - 1}\right) & \lambda > 1 \ . \end{cases}$$

$$(2.45)$$

Dyson Equation

Finally, we can study the effects of the self energy on the Fermi velocity renormalization by means of the Dyson equation [10] [11], i.e.

$$G^{-1}(\mathbf{k}, \omega) = G_0^{-1}(\mathbf{k}, \omega) - \Sigma^{RPA}(\mathbf{k}, \omega) \ . \tag{2.46}$$

In analogy with the Fermi liquid theory [10], we rewrite the the Green's functions by introducing the quasi-particle residue Z, namely

$$G^{-1}(\mathbf{k}, \omega) = Z^{-1}(\Lambda/b)\left(-i\omega\mathbb{1} + Z(\Lambda/b)v_F(\Lambda/b)\mathbf{k} \cdot \boldsymbol{\sigma}\right)$$

$$G_0^{-1}(\mathbf{k}, \omega) = Z^{-1}(\Lambda)\left(-i\omega\mathbb{1} + Z(\Lambda)v_F(\Lambda)\mathbf{k} \cdot \boldsymbol{\sigma}\right) \ ,$$

$$(2.47)$$

with $Z(\Lambda) = 1$. Consequently, defining $r \doteq \Lambda/b$ and $l \doteq log(\Lambda/r)$ as we did in the previous section, the Dyson equation becomes

$$\frac{-i\omega\mathbb{1} + Z(r)v_F(r)\mathbf{k} \cdot \boldsymbol{\sigma}}{Z(r)} = \left(1 + F_{0,\lambda}\frac{8l}{N\pi^2}\right)\left[\frac{-i\omega\mathbb{1}}{Z(\Lambda)} + v_F(\Lambda)\mathbf{k} \cdot \boldsymbol{\sigma}\frac{1 + F_{1,\lambda}\frac{8l}{N\pi^2}}{1 + F_{0,\lambda}\frac{8l}{N\pi^2}}\right]$$

$$\simeq \left(1 + F_{0,\lambda}\frac{8l}{N\pi^2}\right)\left[\frac{-i\omega\mathbb{1}}{Z(\Lambda)} + v_F(\Lambda)\mathbf{k} \cdot \boldsymbol{\sigma}\left(1 + (F_{1,\lambda} - F_{0,\lambda})\frac{8l}{N\pi^2}\right)\right] \ .$$

$$(2.48)$$

In the last line we expanded up to the first order in $1/N$ since we are considering the large fermion flavour limit. From this relation we can derive the RG equations both for $Z(r)$ and $v_F(r)$, namely [4]

$$Z^{-1}(r) = Z^{-1}(\Lambda)\left(1 + F_{0,\lambda}\frac{8l}{N\pi^2}\right) \quad \Rightarrow \quad \frac{dZ}{dl} = -\frac{8}{N\pi^2}F_{0,\lambda}Z \tag{2.49}$$

$$v_F(r) = v_F(\Lambda)\left(1 + (F_{1,\lambda} - F_{0,\lambda})\frac{8l}{N\pi^2}\right) \quad \Rightarrow \quad \frac{dv_F}{dl} = \frac{8}{N\pi^2}(F_{1,\lambda} - F_{0,\lambda})v_F$$

$$(2.50)$$

Renormalization Group Analysis

We can study these solutions both in the strong and weak coupling limit, i.e. for $\lambda \gg 1$ and $\lambda \ll 1$ respectively [4]. In the first case, equations (2.49) and (2.50) go like

$$\frac{dZ}{dl} = -\frac{8}{N\pi^2} \log(2\lambda)Z \qquad \text{and} \qquad \frac{dv_F}{dl} = \frac{8}{N\pi^2}v_F \ ,$$

considering the limit $\lambda \gg 1$ in the integral formulas (2.44) and (2.45). Moreover, we can integrate these equations in the low energy limit, namely for $r \to 0$. For the quasi-particle residue we obtain

$$Z(r) = Z(\Lambda) e^{-\frac{8}{N\pi^2} \log(2\lambda) \log(\Lambda/r)}$$

$$\simeq 1 - \frac{8}{N\pi^2} \log(2\lambda) \log(\Lambda/r) \ ,$$

where we used $Z(\Lambda) = 1$ and we expanded up to the first order in $1/N$. For the Fermi velocity, using $v_F(\Lambda) = v_F$, we get

$$v_F(r) = v_F \left(\frac{\Lambda}{r} \right)^{8/N\pi^2} \ ,$$

which means it is still renormalized towards higher values. Hence, recalling that the electronic charge is RG invariant, we recover the old result for the interaction parameter α, namely it flows to the weak coupling regime. This also implies the quasi-particle residue remains finite due to the competition between the diverging term, $\log(\Lambda/r)$, and the coupling parameter $\log(2\lambda)$, which evolves towards lower values.

In the weak coupling limit, the RG equations (2.49) and (2.50) become

$$\frac{dZ}{dl} = -\frac{8}{N\pi^2} \frac{\lambda^2}{3} Z = -\frac{N\alpha^2}{24} Z \qquad \text{and} \qquad \frac{dv_F}{dl} = \frac{8}{N\pi^2} \frac{\pi\lambda}{4} v_F = \frac{\alpha}{4} v_F \ ,$$

using the definition (2.42) to rewrite the coupling parameter. It is worth noticing that we recovered the old result for the Fermi velocity renormalization, namely equation (2.28), which was obtained for the weak coupling in the first order approximation. We can integrate the quasi-particle residue to get

$$Z(r) = e^{-\frac{N\alpha^2}{24} \log(\Lambda/r)} \simeq 1 - \frac{N\alpha^2}{24} \log\left(\Lambda/r\right) \ ,$$

expanding up to the first order in $N\alpha$.

To sum up, the random phase approximation leads to the same results that we found studying the simpler, first order approximation, namely the weak coupling regime flows to zero. Furthermore, the interesting result comes from the strong coupling analysis. In fact, we observed that even if we start in this regime, i.e. for $\lambda(\Lambda) \gg 1$, the theory flows to weak coupling in the low energy limit, thus the interaction term becomes irrelevant. However, these results were obtained in the large fermion flavour limit, i.e. expanding up to the first order in $1/N$. Even though this is a good approximation to understand the dominant contribution of the polarization function, it may not be good enough to describe the graphene model correctly. Therefore, in the next chapter we will adopt a different prospective to study the spontaneous mass generation, and the consequent finite energy gap.

Chapter 3

Spontaneous Mass Generation

If the electron-electron Coulomb interaction becomes strong enough, a finite energy gap may be opened at the Fermi energy[4][13]. In this chapter, we will test this observation by computing the electron mass as a function of the coupling parameter. We already studied how this phenomenon is prevented in the large fermion flavour limit, in which the theory flows to the weak coupling regime. Hence, we will also analyse how this critical behaviour depends on the electron flavour N[14]. In order to study this process, we will solve the self-consistent Schwinger-Dyson equation[15] both in the low energy limit, in analogy to what we did in the last chapter, and also for the complete Hamiltonian (2.2).

3.1 Charge Density Wave

In the introduction we already explained the motivations that drive us to study the electronic Coulomb interaction specifically. However, it is worth noticing that other kind of interactions may lead to a finite energy gap in the 2D Weyl model. For instance, we could consider the electron-phonon or the spin-orbit coupling, and study their effects on the tight-binding model. Even if we are not doing this, it is worth mentioning that different types of interactions may lead to interesting, non-trivial phases for the graphene lattice.

Going back to the main discussion, we see the mass function can be introduced by looking directly at the non-interacting Bloch Hamiltonian (2.2), namely

$$
\begin{aligned}
h(\mathbf{k}) &= -t \begin{pmatrix} 0 & \sum_{\boldsymbol{\delta}} e^{i\boldsymbol{\delta}\cdot\mathbf{k}} \\ \sum_{\boldsymbol{\delta}} e^{-i\boldsymbol{\delta}\cdot\mathbf{k}} & 0 \end{pmatrix} \\
&= -t \sum_{\boldsymbol{\delta}} \Big(\cos(\mathbf{k}\cdot\boldsymbol{\delta})\sigma_x - \sin(\mathbf{k}\cdot\boldsymbol{\delta})\sigma_y \Big)
\end{aligned}
\tag{3.1}
$$

Thus, we can write the most general gap term as a combination of the Pauli matrices, i.e.

$$\boldsymbol{\Delta} = \Delta_0 \mathbb{1} + (\Delta_x \sigma_x + \Delta_y \sigma_y) + \Delta_z \sigma_Z \ .$$

It is simple to prove that the first contribution would only shift the Dirac cone away from the Fermi level, without affecting its geometry. In the same way,

the central term moves the position of the cone in the momentum space, i.e. it just changes the coordinates of the Dirac points. On the contrary, the last contribution is capable of opening a finite gap, and the corresponding spectrum becomes

$$E_{\pm}(\mathbf{k}) = \pm \sqrt{ \Delta^2(\mathbf{k}) + t^2 \left(3 + 2\cos\left(\sqrt{3}ak_y\right) + 4\cos\left(\frac{\sqrt{3}a}{2}k_y\right)\cos\left(\frac{3a}{2}k_x\right) \right) } .$$

(3.2)

Hence, the energy bands remain gapped as long as the function $\Delta(\mathbf{k})$ is finite.

To understand the physical meaning of this term for the graphene lattice, we start analysing its initial ground state. In the neutral case, the lowest energy is reached when all the carbon atoms are occupied by exactly one valence electron. In this way, in fact, the tight-binding energy is minimised and the two triangular sublattices are equivalent. This is also shown by the Hamiltonian in the coordinate space (2.1), in which the hopping between adjacent sites is equally favoured in both directions. On the contrary, the gap term that we found corresponds to a non-zero value of the order parameter

$$\sum_{\mathbf{k},\alpha} \bar{\Psi}_{\alpha}(\mathbf{k}) \ \Delta(\mathbf{k})\sigma_z \ \Psi_{\alpha}(\mathbf{k}) = \sum_{\mathbf{k},\alpha} \Delta(\mathbf{k})\left(a_{\alpha}^{\dagger}(\mathbf{k})a_{\alpha}(\mathbf{k}) - b_{\alpha}^{\dagger}(\mathbf{k})b_{\alpha}(\mathbf{k}) \right) . \qquad (3.3)$$

The gap function $\Delta(\mathbf{k})$ measures exactly the charge imbalance between the two sublattices, thus determining the formation of a site-centred charge density wave (CDW)[16][17][18]. This means the two sublattices are no longer equivalent, thus the initial lattice symmetry gets broken and a semimetal-insulator phase transition takes place. In particular, the order parameter (3.3) breaks the $U(4)$ chiral symmetry that characterises the initial ground state, hence

$$U(4) \quad \longrightarrow \quad U(2) \otimes U(2) . \qquad (3.4)$$

3.2 Low Energy Analysis

So far, we started from the non-interacting model and studied the perturbation effects of the Coulomb interaction by means of the RG theory. In this chapter, we will no longer threat the electromagnetic contribution as a perturbation, but rather we will consider the strong coupling condition explicitly[13][19]. We expect an energy gap to be opened in this regime, thus we can include it a priori in the model. The idea, in fact, is to assume that a finite gap does exist, and then solve a self-consistent equation to determine its value. In the previous section, we argued which form such a gap function should take, hence we can write the corresponding Green's function as

$$G^{-1}(\mathbf{k}, \omega) = -i\omega \mathbb{1} + v_F \ \mathbf{k} \cdot \boldsymbol{\sigma} + \Delta(|\mathbf{k}|)\sigma_z . \qquad (3.5)$$

For simplicity's sake, we take the mass to be a function of the momentum magnitude only. A more general solution will be discussed later in the chapter when we will analyse the entire Hamiltonian structure. Moreover, we assume

that the RPA interaction satisfies the on-shell condition, thus equation (2.38) becomes

$$V^{RPA}(\mathbf{k}, \omega = v_F|\mathbf{k}|) = \frac{2\pi e^2}{\left(4\pi\epsilon + \frac{\sqrt{2}N\pi e^2}{16 v_F}\right)|\mathbf{k}|} \ . \tag{3.6}$$

It is worth noticing that we will consider here the random phase approximation even though the large fermion flavour limit is no longer applied. In fact, this is a good approximation as long as $N > 1$, which is the case of the model considered.

The interacting Green's function can be related to the system by means of the Schwinger-Dyson equation[15][19] i.e.

$$G^{-1}(\mathbf{k}, \omega) = G_0^{-1}(\mathbf{k}, \omega) + \int \frac{d\mathbf{p}}{(2\pi)^2} \frac{d\nu}{2\pi} V(\mathbf{k} + \mathbf{p}, \omega + \nu) G(\mathbf{p}, \nu) \ . \tag{3.7}$$

This is a self-consistent equation that connects the Green's function to the system interaction. In our case, the potential is given by $V^{RPA}(\mathbf{k}, \omega = v_F|\mathbf{k}|)$, and the Green's function follows from equation (3.5), namely

$$G(\mathbf{k}, \omega) = \frac{i\omega\mathbb{1} + v_F\mathbf{k}\cdot\boldsymbol{\sigma} + \Delta(|\mathbf{k}|)\sigma_z}{\omega^2 + v_F^2|\mathbf{k}|^2 + \Delta^2(|\mathbf{k}|)} \ . \tag{3.8}$$

Hence, we can obtain an expression for the gap function by multiplying both sides of (3.7) by σ_z, and then taking the trace, i.e.

$$\Delta(|\mathbf{k}|) = \int_0^\Lambda \frac{d\mathbf{p}}{(2\pi)^2} \int_{-\infty}^\infty \frac{d\nu}{2\pi} \frac{v_F}{\left(\frac{4\pi\epsilon v_F}{2\pi e^2} + \frac{N}{16\sqrt{2}}\right)|\mathbf{k} + \mathbf{p}|} \frac{\Delta(|\mathbf{p}|)}{\nu^2 + v_F^2|\mathbf{p}|^2 + \Delta^2(|\mathbf{p}|)} \ . \tag{3.9}$$

This is a self-consistent equation for the energy gap in the linear regime. The goal is to solve it numerically to find its non-trivial solutions, which thus correspond to a finite gap at the Dirac points. We can simplify this expression by defining a new parameter

$$\lambda(\alpha, N) \doteq \frac{1}{4\pi} \frac{1}{\left(\frac{4\pi\epsilon v_F}{2\pi e^2} + \frac{N}{16\sqrt{2}}\right)} = \frac{1}{4\pi} \frac{1}{\frac{1}{2\pi\alpha} + \frac{N}{16\sqrt{2}}} \ , \tag{3.10}$$

where we used the coupling parameter definition (2.25). Furthermore, we can integrate out the frequency dependence by using the residue theorem, i.e.

$$\int_{-\infty}^\infty \frac{d\nu}{2\pi} \frac{1}{\nu^2 + v_F^2|\mathbf{p}|^2 + \Delta^2(|\mathbf{p}|)} = \frac{1}{2\sqrt{v_F^2|\mathbf{p}|^2 + \Delta^2(|\mathbf{p}|)}} \ . \tag{3.11}$$

Finally, we redefine the gap as $\Delta' \to \Delta/v_F$, namely in such a way that the expression becomes formally independent on the Fermi velocity. In the end the self-consistent gap equation becomes

$$\Delta(|\mathbf{k}|) = \int_0^\Lambda \frac{d\mathbf{p}}{2\pi} \frac{\lambda}{|\mathbf{k} + \mathbf{p}|} \frac{\Delta(|\mathbf{p}|)}{\sqrt{|\mathbf{p}|^2 + \Delta^2(|\mathbf{p}|)}} \ . \tag{3.12}$$

3.2.1   Numerical Results

The equation (3.12) can be solved numerically for different values of the coupling function $\lambda(\alpha, N)$[19]. First of all, we can work out the angular dependence by introducing the polar coordinates, hence the integral over the angular contribution becomes

$$
\begin{aligned}
f_{\mathbf{k}}(\mathbf{p}) &= \int_0^{2\pi} d\theta \frac{1}{\sqrt{|\mathbf{p}|^2 + |\mathbf{k}|^2 + 2|\mathbf{p}||\mathbf{k}|\cos\theta}} \\[2mm]
&= \frac{1}{\sqrt{|\mathbf{p}|^2 + |\mathbf{k}|^2}} \int_0^{2\pi} d\theta \frac{1}{\sqrt{1 + \frac{2|\mathbf{p}||\mathbf{k}|}{|\mathbf{p}|^2+|\mathbf{k}|^2}\left(1 - 2\sin^2(\theta/2)\right)}} \\[2mm]
&= \frac{4}{\sqrt{|\mathbf{p}|^2 + |\mathbf{k}|^2}} \int_0^{\pi/2} d\phi \frac{1}{\sqrt{1 + \frac{2|\mathbf{p}||\mathbf{k}|}{|\mathbf{p}|^2+|\mathbf{k}|^2}\left(1 - 2\sin^2(\phi)\right)}} \\[2mm]
&= \frac{4}{\sqrt{|\mathbf{p}|^2 + |\mathbf{k}|^2}} \frac{1}{\sqrt{1 + \frac{2|\mathbf{p}||\mathbf{k}|}{|\mathbf{p}|^2+|\mathbf{k}|^2}}} \int_0^{\pi/2} d\phi \frac{1}{\sqrt{1 - \frac{4|\mathbf{p}||\mathbf{k}|}{|\mathbf{p}|^2+|\mathbf{k}|^2}\sin^2(\phi)}} \\[2mm]
&= \frac{4}{|\mathbf{p}| + |\mathbf{k}|} K\left(\frac{4|\mathbf{p}||\mathbf{k}|}{|\mathbf{p}|^2 + |\mathbf{k}|^2}\right) .
\end{aligned}
\tag{3.13}
$$

In the last line we used the definition of the elliptic integral of the first kind $K(x)$. The gap equation is now expressed as a function of the momentum magnitude alone. The integral runs from 0 up to the cut-off $\Lambda = 1/a$, which can be set to 1 in the numerical integration.

The solution can be found by using a recursive method, i.e. integrating until the new solution differs from the old one by less than a fixed cutoff ϵ (see Appendix B). In particular, inserting the angular integral (3.13) into the Schwinger-Dyson equation (3.12), we can write the n-th recursive step as

$$
\Delta_n(|\mathbf{k}|) = \frac{\lambda}{2\pi} \int_0^\Lambda dp \, \frac{4p}{p + |\mathbf{k}|} \frac{\Delta_{n-1}(p)}{\sqrt{p^2 + \Delta_{n-1}^2(p)}} K\left(\frac{4p|\mathbf{k}|}{p^2 + |\mathbf{k}|^2}\right) .
\tag{3.14}
$$

In this way, we can find two distinct approximations of the exact solution, which we know it will be enclosed between them. In fact, when we start from an initial guess for the gap function, the numerical solution will approach the exact result without actually reaching it. Hence, the exact solution satisfies

$$
\Delta_{\lambda,1}^{ansatz} < \Delta_{\lambda,1}^{num} < \Delta_\lambda^{exact} < \Delta_{\lambda,2}^{num} < \Delta_{\lambda,2}^{ansatz} .
\tag{3.15}
$$

This method has two important consequences. First of all, it allows to estimate the numerical error for each solution, which is related to the cutoff ϵ in a non-trivial way. Secondly, we can use it to find the critical parameter λ_c, below which there is no finite solution. In fact, if the numerical result is lower than the initial ansatz regardless the function that starts the recursive algorithm, this implies there is not a region that contains the exact result, namely the equation admits only the trivial solution.
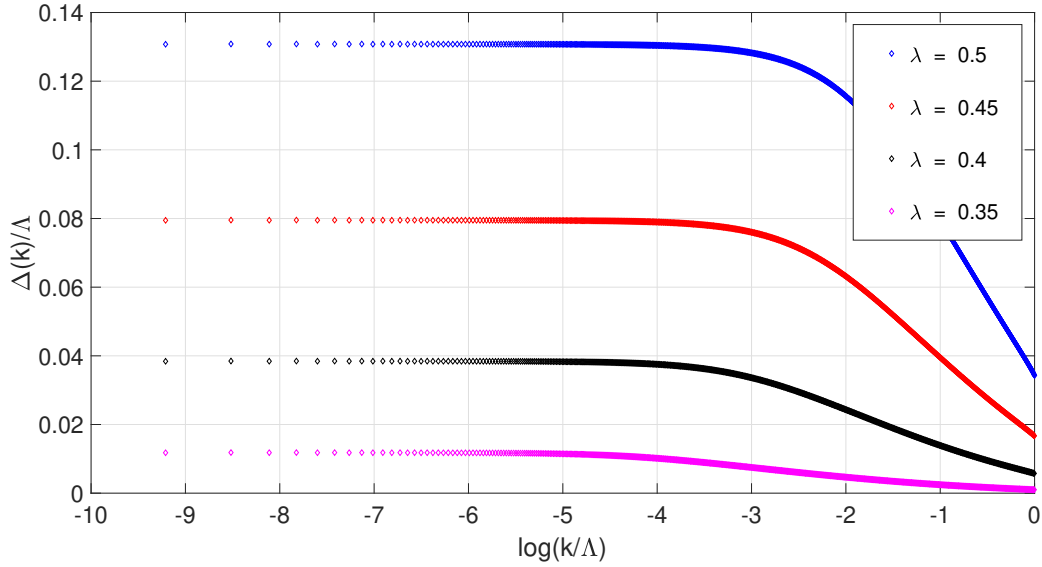
Figure 3.1: Mass gap in the strong coupling regime. The electrons acquire a finite mass around the Dirac points, i.e. for $|\mathbf{k}| \to 0$ (left portion of the domain).

The first important result comes from the strong coupling regime. If λ is large enough, in fact, we see that a non-trivial solution of the gap equation exists. This confirms our initial hypothesis about the possibility to open an energy gap by means of the Coulomb interaction.

If we further decrease the coupling parameter, we quickly reach a region where the gap function becomes small. In particular, we estimate the critical value of the coupling parameter at $\lambda_c = 0.272$, below which it is not possible to find a non-trivial solution for the mass.
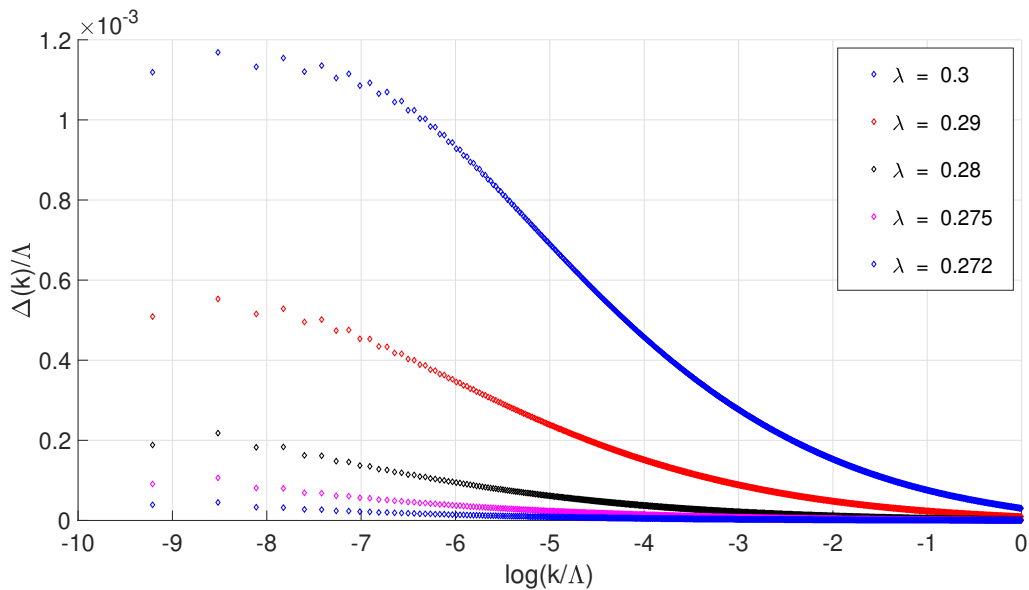

Figure 3.2: Mass gap in the critical region. We see the numerical solution becomes more unstable when we approach this regime.

3.2.2   Semimetal-Insulator Phase Transition

We can combine the critical value that we found in the last section, i.e. $\lambda_c = 0.272$, with its definition (3.10). In this way, we derive a relationship between the critical coupling parameter, α_c, and the fermion flavour, namely

$$\alpha_c = \frac{2\lambda_c}{1 - \frac{\pi N}{4\sqrt{2}}\lambda_c} \quad \text{with} \quad \lambda_c = 0.272 \ . \tag{3.16}$$

We can plot this result in the $\alpha_c - N$ plane (see Fig. 3.3). This phase diagram shows that if the coupling constant of the material lies above the critical line (blue line in Fig. 3.3), then a semimetal-insulator phase transition[14] should take place. It is worth noticing that this diagram admits a maxim value for the electron flavour, beyond which the material remains gapless regardless the coupling strength. This agrees with the result that comes from the RG analysis. In fact, in the last chapter we found that the theory flows to the weak coupling regime in the limit of large fermion flavour.

For $N = 4$, which corresponds to the graphene model, the critical coupling parameter is $\alpha_c(N = 4) = 1.37$. The value for pristine monolayer graphene is about $\alpha_{graphene} = 2.16$[20], thus we expect the actual ground state to be gapped. However, the simple theory that we used to describe the graphene model does not include lots of important contributions, which may affect the gap value that we found. Moreover, the measure is made difficult by other effects that we did not consider in our theory, such as the thermal fluctuations that play a crucial role in experiments like these. In the next section, we will propose a more complete description of the problem, which overcomes some of the structural concerns listed here.
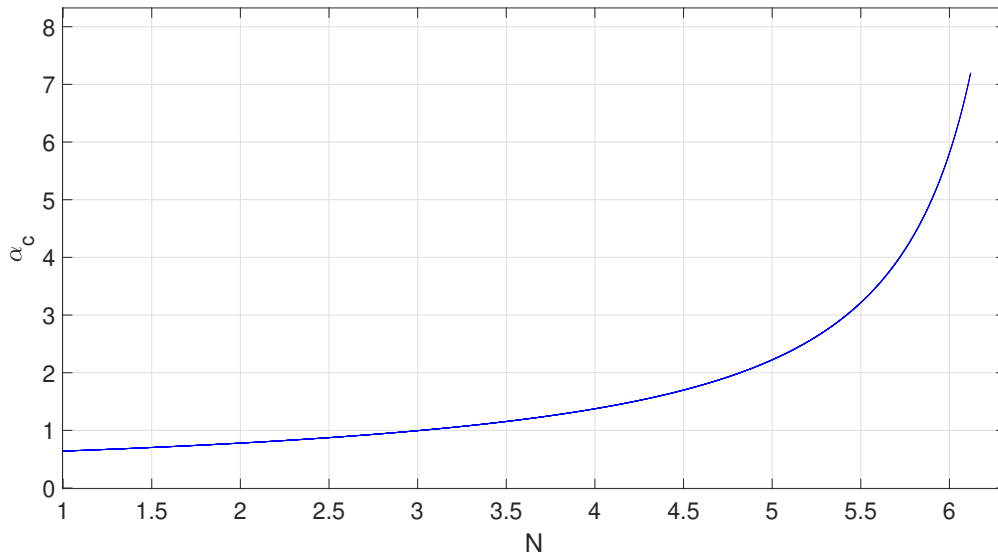

Figure 3.3: Phase diagram of 2D Weyl semimetals in the $\alpha_c - N$ plane. Above the blue line the material is an insulator, below it is a semimetal.

3.3 Complete Hamiltonian Approach

In this section we will study the energy gap for the entire graphene lattice. In this way, our derivation will no longer depend on the momentum cutoff, and all the effects given by the non-linear contributions will be automatically included. However, this method does not allow to study the general 2D Weyl semimetal with electron flavour N, but it is specific for the lattice in exam. Further motivations for this method will become clear in the next chapter, when it will be applied to study the Kagome lattice.

3.3.1 Polarization Function

The non-interacting Green's function is obtained by substituting the tight-binding Hamiltonian (3.1) into the free action (2.7), namely

$$G_0^{-1}(\mathbf{k}, \omega) = -i\omega \mathbb{1} - t \sum_{\boldsymbol{\delta}} \left(\cos(\mathbf{k} \cdot \boldsymbol{\delta})\sigma_x - \sin(\mathbf{k} \cdot \boldsymbol{\delta})\sigma_y \right) \qquad (3.17)$$

$$G_0(\mathbf{k}, \omega) = \frac{i\omega \mathbb{1} - t \sum_{\boldsymbol{\delta}} \left(\cos(\mathbf{k} \cdot \boldsymbol{\delta})\sigma_x - \sin(\mathbf{k} \cdot \boldsymbol{\delta})\sigma_y \right)}{\omega^2 + t^2 \sum_{\boldsymbol{\delta}, \boldsymbol{\delta}'} e^{i\mathbf{k} \cdot (\boldsymbol{\delta} - \boldsymbol{\delta}')}} \; . \qquad (3.18)$$

The second expression can be used to compute the polarization function shown in Fig. 2.5. In this case, the two independent Dirac points are both included in the structure of (3.18). However, the form of the tight-binding Hamiltonian (2.2) highlights that we are not including the spin contribution in our model, thus we need to introduce its degeneracy manually. Hence, the polarization function becomes

$$\Pi(\mathbf{k}, \omega) = 2 \int \frac{d\nu}{2\pi} \frac{d\mathbf{q}}{(2\pi)^2} \, Tr \left(G_0 \left(\mathbf{k} + \mathbf{q}, \omega + \nu \right) G_0 \left(\mathbf{q}, \nu \right) \right) \; , \qquad (3.19)$$

where the general fermion flavour N that appears in (2.32) is substituted by the two-fold spin degeneracy. The important difference with respect to the linear case is that now the momentum integration runs over the first Brillouin zone, rather than a disk of radius Λ. Working out the trace that appears in the expression (3.19), the polarization can be written as

$$\Pi(\mathbf{k}, \omega) = -4 \int \frac{d\nu}{2\pi} \frac{d\mathbf{q}}{(2\pi)^2} \frac{\nu(\nu + \omega) - t^2 \sum_{\boldsymbol{\delta}, \boldsymbol{\delta}'} \cos \left(\mathbf{k} \cdot \boldsymbol{\delta} + \mathbf{q} \cdot (\boldsymbol{\delta} - \boldsymbol{\delta}') \right)}{\left[(\nu + \omega)^2 + t^2 \sum_{\boldsymbol{\delta}, \boldsymbol{\delta}'} e^{i(\mathbf{q} + \mathbf{k}) \cdot (\boldsymbol{\delta} - \boldsymbol{\delta}')} \right] \left[\nu^2 + t^2 \sum_{\boldsymbol{\delta}, \boldsymbol{\delta}'} e^{i\mathbf{q} \cdot (\boldsymbol{\delta} - \boldsymbol{\delta}')} \right]} \; . \qquad (3.20)$$

The integral over ν can be performed as usual by means of the residue theorem. The resulting expression is integrated numerically using the Gaussian quadrature method (see Appendix B). To deal with the frequency dependence, we solve this integral with the on-shell condition, i.e. for $\omega = v_F |\mathbf{k}|$. The Fermi velocity comes out from setting the lattice constant to one, hence making the hopping parameter proportional to the Fermi velocity according to $v_F = \frac{3}{2}t$. This is consistent with the theory since the action of the Coulomb interaction does not affect the geometrical structure of graphene, hence it does non change the lattice constant. The polarization function (3.20) results proportional to

the hopping parameter, similarly to the linear approximation result (2.37), which goes like $1/v_F$ within the on-shell condition. Hence, we can define the function $\tilde{\Pi}(\mathbf{k}, \omega' = \omega/t) \doteq t\Pi(\mathbf{k}, \omega)$, that results independent on the hopping parameter value. The numerical result for this reparametrized polarization function is shown in Fig. 3.4.
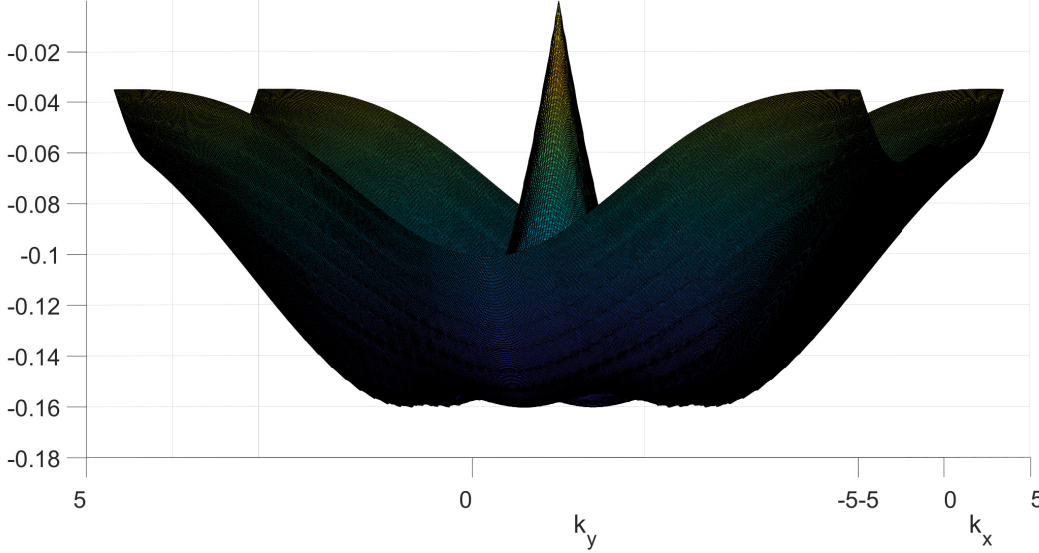

Figure 3.4: Polarization function for the graphene lattice within the on-shell condition.

It is worth noticing that in the low energy regime, i.e. for $(\mathbf{k}, \omega) \to 0$, we recover the result found in the linear approximation given by equation (2.37).

3.3.2   Schwinger-Dyson Equation

The interacting Green's function is given by (3.18) plus the gap term that produces the CDW ground state, i.e. $\Delta(\mathbf{k})\sigma_z$. In this case, we consider the mass to be a function of the momentum vector, thus it is defined over the entire Brillouin zone. We can multiply the Schwinger-Dyson equation by σ_z and then take the trace to work out an expression for the gap function, namely

$$\Delta(\mathbf{k}) = \int \frac{d\mathbf{p}}{(2\pi)^2} \frac{d\nu}{2\pi} \, V^{RPA}(\mathbf{k} + \mathbf{p}, \omega + \nu) \frac{\Delta(\mathbf{p})}{\nu^2 + \Delta^2(\mathbf{p}) + t^2 \sum_{\boldsymbol{\delta}, \boldsymbol{\delta}'} e^{i\mathbf{p}\cdot(\boldsymbol{\delta} - \boldsymbol{\delta}')}} \, .$$
(3.21)

The RPA potential within the on-shell condition is derived from the diagrammatic equation in Fig. 2.6, i.e.

$$V^{RPA}(\mathbf{k}, \omega = v_F|\mathbf{k}|) = \frac{1}{\frac{4\pi\epsilon|\mathbf{k}|}{2\pi e^2} - \Pi(\mathbf{k}, \omega = v_F|\mathbf{k}|)}$$

$$= \frac{v_F}{\frac{|\mathbf{k}|}{2\pi\alpha} - \frac{3}{2}\tilde{\Pi}(\mathbf{k}, \omega = 3|\mathbf{k}|/2)} \, .$$
(3.22)

At this point we can use equation (3.11) to integrate the frequency. Moreover, we can rewrite the sum using the definition of the nearest neighbour vectors, namely

$$g(\mathbf{p}) \doteq \sum_{\boldsymbol{\delta}, \boldsymbol{\delta}'} e^{i\mathbf{p} \cdot (\boldsymbol{\delta} - \boldsymbol{\delta}')}$$

$$= 3 + 2 \left[\cos \left(\sqrt{3} a p_y \right) + 2 \cos \left(\frac{3a}{2} p_x \right) \cos \left(\frac{\sqrt{3}a}{2} p_y \right) \right] \ .$$

Lastly, we can use the same reparametrization that we applied in the linear regime, i.e. $\Delta' \to \Delta/v_F$. In this way, equation (3.21) becomes

$$\Delta(\mathbf{k}) = \int_{BZ} \frac{d\mathbf{p}}{(2\pi)^2} \ \frac{1}{\frac{|\mathbf{k}+\mathbf{p}|}{2\pi\alpha} - \frac{3}{2}\tilde{\Pi}(\mathbf{k}+\mathbf{p})} \frac{\Delta(\mathbf{p})}{2\sqrt{\Delta^2(\mathbf{p}) + \frac{4}{9}g(\mathbf{p})}} \ , \tag{3.23}$$

which can be solved numerically for different values of the coupling parameter α.

3.3.3 Numerical Results

The gap equation (3.23) can be integrated using the Gaussian quadrature method. In particular, we use the same recursive procedure presented in the linear expansion analysis. For each value of the coupling parameter, we find a similar profile for the mass equation over the first Brillouin zone. An example of the solution is given in Fig. 3.5.
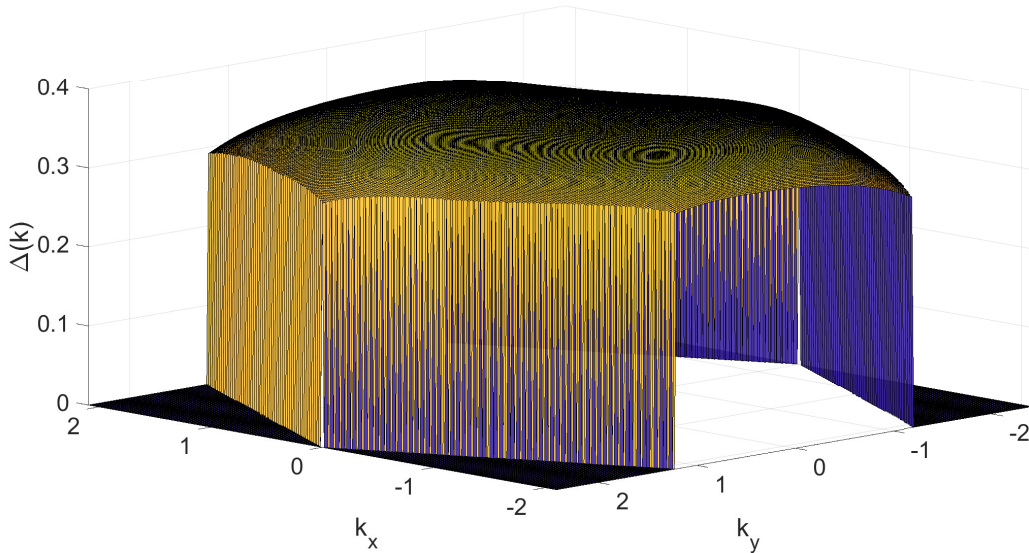

Figure 3.5: Numerical solution of the gap equation (3.23) with coupling parameter $\alpha = 2.0$.

At this point, we can derive the semimetal-insulator phase diagram by computing the energy gap as a function of the coupling parameter (see Fig. 3.6). In fact, we saw at the beginning of the chapter that the mass function can be

thought as the order parameter that leads to a charge imbalance of the neutral ground state. Thus, according to Landau's classification, we find a continuous phase transition that breaks the chiral symmetry of the system. The critical coupling parameter is $\alpha_c = 1.333$, which is similar to the result that we found with the linear expansion. The difference between the two results is due to the non-linear contributions that we automatically included in this second derivation.
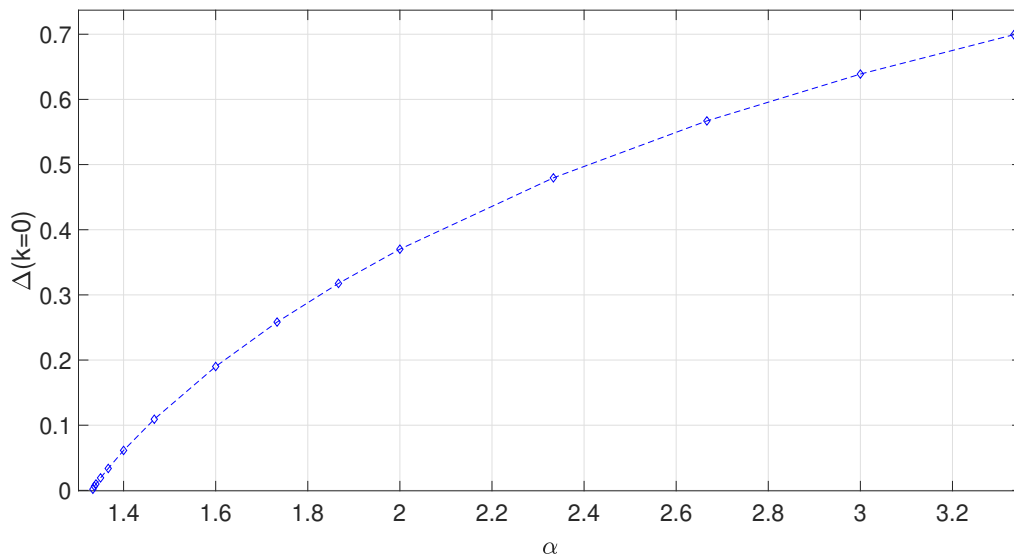

Figure 3.6: Mass gap as a function of the coupling parameter α.

Chapter 4

Kagome Lattice

In this chapter, we will study the effects of the Coulomb interaction on the Kagome lattice[5][6][21][22]. We will use the same techniques that we presented so far in our analysis, namely studying the Schwinger-Dyson equation within the random phase approximation. Particular attention will be paid to evidence the parallelisms and differences between this novel material and graphene.

We already discussed in the introduction that the Kagome metals have been suggested to be a valid alternative to graphene in the study of electron hydro-dynamics[8]. In fact, we saw how this phenomenon is favoured by the strong coupling that takes place in these materials. However, it should be clear at this point that enhancing the effects of the Coulomb interaction may lead to significant consequences on the energy structure of 2D Weyl semimetals. The goal of this chapter is to address this question quantitatively, aiming to prove whether this novel material could represent a revolutionary step forward in the electron hydrodynamics field.

4.1 Tight-binding Model

The Kagome lattice is also composed by identical atoms arranged in a 2D hexagonal structure. However, unlike graphene, these are positioned along the edges rather than the vertices of the hexagons (see Fig. 4.1). Consequently, each atom has four nearest neighbour sites rather than just three, hence we need three distinct sublattices to describe the entire structure. In particular, the lattice vectors that compose each of these sublattices A, B and C are given by

$$\mathbf{a}_1 = a\left(2, 0\right) , \quad \mathbf{a}_2 = a\left(1, \sqrt{3}\right) , \quad \mathbf{a}_3 = a\left(-1, \sqrt{3}\right) . \qquad (4.1)$$

Hence, each atom is surrounded by other four atoms positioned at $\pm\mathbf{a}_i/2$ for $i = 2, 3$.

We assume here that each atom contributes to the electronic structure with exactly one valence electron. Moreover, we take into account only the nearest neighbour hopping, thus excluding the possibility for next nearest or longer exchanges. In fact, we already argued that this is a good approximation for the phenomena that we aim to study here. The tight-binding Hamiltonian
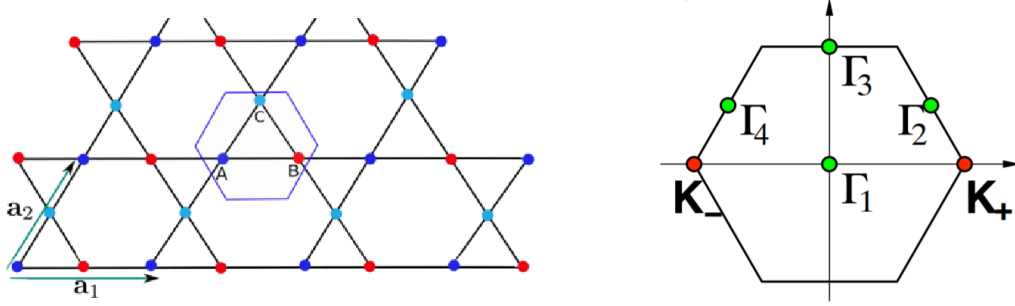
Figure 4.1: (Left) : Lattice structure of Kagome. The sublattices, A, B and C, are described by the lattice unit vectors $\mathbf{a}_1$ and $\mathbf{a}_2$, and they are connected by the nearest neighbour vectors $\boldsymbol{\delta}_i$ (adapted from[23]). (Right) The corresponding Brillouin zone. The two independent Dirac points are located at $\mathbf{K}_-$ and $\mathbf{K}_+$ (adapted from[6]).

then becomes

$$H = -t \sum_{<i,j,l>,\sigma} \left(a^\dagger_{\sigma,i} b_{\sigma,j} + a^\dagger_{\sigma,i} c_{\sigma,l} + b^\dagger_{\sigma,j} c_{\sigma,l} + h.c. \right) \ . \tag{4.2}$$

Here $a^\dagger_{\sigma,i}(a_{\sigma,i})$ creates(annihilates) an electron with spin σ on site i on sublattice A, t is the hopping parameter, and the sum is taken over the nearest neighbour sites only. We can now transform the Hamiltonian to the momentum space in analogy to what we did for the graphene lattice, i.e. by Fourier transforming the operators as

$$a^\dagger_i = \frac{1}{\sqrt{N/3}} \sum_{\mathbf{k}} e^{-i\mathbf{k}\cdot\mathbf{r}_i} a^\dagger(\mathbf{k}) \qquad \text{and} \qquad a_i = \frac{1}{\sqrt{N/3}} \sum_{\mathbf{k}} e^{i\mathbf{k}\cdot\mathbf{r}_i} a(\mathbf{k}) \ . \tag{4.3}$$

Equivalent expressions can be written down also for the sublattices B and C by transforming the operators $b^\dagger_j(b_j)$ and $c^\dagger_l(c_l)$ respectively. Moreover, we can rewrite the vector positions on the sublattices B and C by using the lattice vectors (4.1), namely $\mathbf{r}_j = \mathbf{r}_i \pm \boldsymbol{\delta}_{12}$ and $\mathbf{r}_l = \mathbf{r}_i \pm \boldsymbol{\delta}_{13}$, where $i \in A$, $j \in B$, $l \in C$ and

$$\boldsymbol{\delta}_{12} = \frac{a}{2}\left(-1, \sqrt{3}\right) \quad \boldsymbol{\delta}_{13} = \frac{a}{2}\left(1, \sqrt{3}\right) \ . \tag{4.4}$$

Hence, the spinless Hamiltonian becomes

$$H_\sigma = -t \sum_{i \in A} \sum_{\mathbf{k},\mathbf{k}'} \frac{1}{N/3} \left(e^{-i\mathbf{r}_i \cdot (\mathbf{k}-\mathbf{k}')} e^{i\mathbf{k}' \cdot \boldsymbol{\delta}_{12}} a^\dagger(\mathbf{k}) b(\mathbf{k}') + e^{-i\mathbf{r}_i \cdot (\mathbf{k}-\mathbf{k}')} e^{-i\mathbf{k}' \cdot \boldsymbol{\delta}_{12}} a^\dagger(\mathbf{k}) b(\mathbf{k}') \right.$$

$$+ e^{-i\mathbf{r}_i \cdot (\mathbf{k}-\mathbf{k}')} e^{i\mathbf{k}' \cdot \boldsymbol{\delta}_{13}} a^\dagger(\mathbf{k}) c(\mathbf{k}') + e^{-i\mathbf{r}_i \cdot (\mathbf{k}-\mathbf{k}')} e^{-i\mathbf{k}' \cdot \boldsymbol{\delta}_{13}} a^\dagger(\mathbf{k}) c(\mathbf{k}') + e^{-i\mathbf{r}_i \cdot (\mathbf{k}-\mathbf{k}')}$$

$$e^{-i\mathbf{k} \cdot \boldsymbol{\delta}_{12}} e^{i\mathbf{k}' \cdot \boldsymbol{\delta}_{13}} b^\dagger(\mathbf{k}) c(\mathbf{k}') + e^{-i\mathbf{r}_i \cdot (\mathbf{k}-\mathbf{k}')} e^{i\mathbf{k} \cdot \boldsymbol{\delta}_{12}} e^{-i\mathbf{k}' \cdot \boldsymbol{\delta}_{13}} b^\dagger(\mathbf{k}) c(\mathbf{k}') + h.c. \left. \right)$$

$$= -t \sum_{i \in A} \sum_{\mathbf{k},\mathbf{k}'} \frac{1}{N/3} \left(2\cos\left(\mathbf{k}' \cdot \boldsymbol{\delta}_{12}\right) e^{-i\mathbf{r}_i \cdot (\mathbf{k}-\mathbf{k}')} a^\dagger(\mathbf{k}) b(\mathbf{k}') + 2\cos\left(\mathbf{k}' \cdot \boldsymbol{\delta}_{13}\right) \right.$$

$$e^{-i\mathbf{r}_i \cdot (\mathbf{k}-\mathbf{k}')} a^\dagger(\mathbf{k}) c(\mathbf{k}') + 2\cos\left(\mathbf{k} \cdot \boldsymbol{\delta}_{12} - \mathbf{k}' \cdot \boldsymbol{\delta}_{13}\right) e^{-i\mathbf{r}_i \cdot (\mathbf{k}-\mathbf{k}')} b^\dagger(\mathbf{k}) c(\mathbf{k}') + h.c. \left. \right)$$

$$= -2t \sum_{\mathbf{k}} \left(\cos\left(\mathbf{k} \cdot \boldsymbol{\delta}_{12}\right) a^\dagger(\mathbf{k}) b(\mathbf{k}) + \cos\left(\mathbf{k} \cdot \boldsymbol{\delta}_{13}\right) a^\dagger(\mathbf{k}) c(\mathbf{k}) + \cos\left(\mathbf{k} \cdot \boldsymbol{\delta}_{23}\right) \right.$$

$$b^\dagger(\mathbf{k}) c(\mathbf{k}) + h.c. \left. \right) ,$$

$$(4.5)$$

where we used that $\sum_{i \in A} e^{i\mathbf{r}_i \cdot (\mathbf{k}-\mathbf{k}')} = \frac{N}{3} \delta\left(\mathbf{k} - \mathbf{k}'\right)$, and we defined the vector connecting the B and C sublattice as

$$\boldsymbol{\delta}_{23} = \boldsymbol{\delta}_{13} - \boldsymbol{\delta}_{12} = a\left(1, 0\right) . \qquad (4.6)$$

At this point, we can define the total creation and annihilation operator as, respectively, $\bar{\Psi}_\sigma(\mathbf{k}) = \begin{pmatrix} a_\sigma^\dagger(\mathbf{k}) & b_\sigma^\dagger(\mathbf{k}) & c_\sigma^\dagger(\mathbf{k}) \end{pmatrix}$ and $\Psi_\sigma(\mathbf{k}) = (a_\sigma(\mathbf{k}) \quad b_\sigma(\mathbf{k}) \quad c_\sigma(\mathbf{k}))^T$. Hence, the tight-binding Hamiltonian transformed in the momentum space becomes[6]

$$H = -2t \sum_{\sigma,\mathbf{k}} \bar{\Psi}_\sigma(\mathbf{k}) \begin{pmatrix} 0 & \cos(\mathbf{k} \cdot \boldsymbol{\delta}_{12}) & \cos(\mathbf{k} \cdot \boldsymbol{\delta}_{13}) \\ \cos(\mathbf{k} \cdot \boldsymbol{\delta}_{12}) & 0 & \cos(\mathbf{k} \cdot \boldsymbol{\delta}_{23}) \\ \cos(\mathbf{k} \cdot \boldsymbol{\delta}_{13}) & \cos(\mathbf{k} \cdot \boldsymbol{\delta}_{23}) & 0 \end{pmatrix} \Psi_\sigma(\mathbf{k}) . \quad (4.7)$$

The energy spectrum is given by the eigenvalues of the Bloch Hamiltonian in (4.7), i.e.

$$\begin{cases} E_{1,2}(\mathbf{k}) = -t \left(1 \pm \sqrt{3 + 2 \sum_j \cos(2\mathbf{k} \cdot \boldsymbol{\delta}_j)} \right) \\ E_3(\mathbf{k}) = 2t \end{cases} \qquad (4.8)$$

which is shown in Fig. 4.2. Compared to the graphene spectrum, Kagome's is composed by two bands which recall the old structure, plus an additional flat band sitting on top. In principle, we might expect this flat band to play a relevant role in the spontaneous mass generation. Thus, studying the entire

Hamiltonian as we did for graphene allows to include automatically all the effects due to the coupling between the flat band and the low energy expansion at the Dirac points. The two non-flat energy bands touch each other at the Dirac points, which are located at

$$\mathbf{K}_D = \left(\frac{2\pi}{3a}, 0\right) \qquad \mathbf{K}'_D = \left(-\frac{2\pi}{3a}, 0\right) \ . \tag{4.9}$$
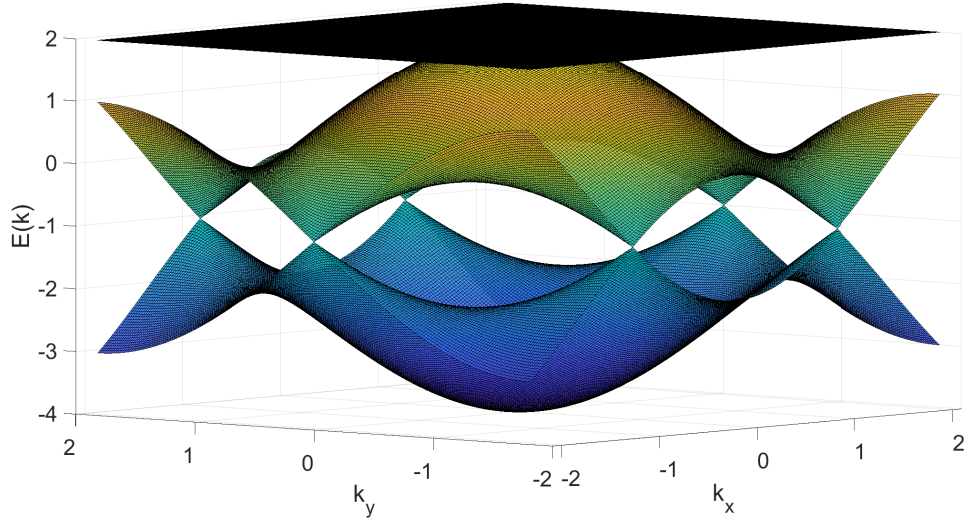

Figure 4.2: Energy spectrum of the non-interacting Kagome model (in units of the hopping parameter t).

4.1.1   Low Energy Expansion

In the graphene lattice, the two energy bands that compose the non-interacting ground state result naturally decoupled. In other words, it is sufficient to expand the Bloch Hamiltonian around one of the two independent Dirac point in order to obtain the linear Dirac cone structure that determines the massless electron dispersion. For the Kagome lattice, the picture seems different since the tight-binding model (4.7) does not show the same simple structure. In fact, if we expand the Bloch Hamiltonian up to the first order in $|\mathbf{q}|/|\mathbf{K}_D|$ we get

$$h(\mathbf{q}) \simeq -t \begin{pmatrix} 0 & 1 - \frac{\sqrt{3}}{2}aq_x + \frac{3}{2}aq_y & 1 - \frac{\sqrt{3}}{2}aq_x - \frac{3}{2}aq_y \\ 1 - \frac{\sqrt{3}}{2}aq_x + \frac{3}{2}aq_y & 0 & -1 - \sqrt{3}aq_x \\ 1 - \frac{\sqrt{3}}{2}aq_x - \frac{3}{2}aq_y & -1 - \sqrt{3}aq_x & 0 \end{pmatrix} \ .$$

We can find a unitary transformation matrix that is able to decouple the three energy levels at the Dirac point. This is done by taking a set of orthogonal eigenvectors of the liner Hamiltonian $h(\mathbf{q} = 0)$ corresponding to the different bands. However, we need to work out a combination of eigenstates that is able

to preserve the Hermitian structure of the initial matrix. For example, this can be achieved by

$$U = \left[\frac{1}{\sqrt{2}} \begin{pmatrix} 0 \\ 1 \\ -1 \end{pmatrix} \, , \, \frac{1}{\sqrt{6}} \begin{pmatrix} 2 \\ 1 \\ 1 \end{pmatrix} \, , \, \frac{1}{\sqrt{3}} \begin{pmatrix} -1 \\ 1 \\ 1 \end{pmatrix} \right] \, . \tag{4.10}$$

In this way, the linear expansion matrix transforms into

$$U^{-1} \, h(\mathbf{q}) \, U = t \begin{pmatrix} -1 - \sqrt{3}aq_x & -\sqrt{3}aq_y & \sqrt{\frac{3}{2}}aq_y \\ -\sqrt{3}aq_y & -1 + \sqrt{3}aq_x & \sqrt{\frac{3}{2}}aq_x \\ \sqrt{\frac{3}{2}}aq_y & \sqrt{\frac{3}{2}}aq_x & 2 \end{pmatrix} \, . \tag{4.11}$$

The 2x2 matrix at the upper-left corner recalls exactly the structure of the graphene linear expansion. The other terms are due to the flat band contribution at the Dirac point, i.e. the third diagonal term with corresponding energy $2t$, plus the remaining bands coupling in the vicinity of the Dirac point. In fact, the decoupling process is not exact since we have considered $h(\mathbf{q} = 0)$ to work out the transformation matrix U. In principle, we could derive a unitary transformation that depends explicitly on the momentum and that is is able to decouple the flat band in the whole linear regime. However, this becomes exponentially more expensive in terms of computational time, and it does not have relevant consequences to our current discussion. Thus, focusing on the 2x2 submatrix, we can write down the linear theory in the low energy expansion, namely

$$h^{linear}(\mathbf{q}) = -t \begin{pmatrix} 1 + \sqrt{3}aq_X & \sqrt{3}aq_y \\ \sqrt{3}aq_y & 1 - \sqrt{3}aq_x \end{pmatrix} = \mu + v_F \left(q_x \sigma_z + q_y \sigma_x \right) \, . \tag{4.12}$$

Here μ is the chemical potential at the Dirac point and $v_F = \sqrt{3}at$ is the Kagome Fermi velocity. The important result is that we recovered the same linear dispersion that we had found for the graphene lattice. Hence, we see that ignoring completely the additional flat band, the Kagome analysis would coincide perfectly with the derivation in section (3.2). Naturally, this result could have been understood directly from the energy structure (4.8). However, this derivation allows us to introduce the Fermi velocity in analogy to what we did for graphene, and also it will represent the starting point of the next section.

4.2 Dimerization

The central question now is how can we open an energy gap at the Dirac points of the Kagome lattice? The first step could be to take the linearized Hamiltonian (4.12) and introduce a mass term in analogy to what we did for graphene. It is worth noticing that now the electron momentum is proportional to the Pauli matrices along the $x-$ and $z-$direction, thus the gap function should look like $\mathbf{\Delta}_{lin}(\mathbf{k}) = \Delta_{lin}(\mathbf{k})\sigma_y$. If we now use the unitary matrix U to

transform the interacting contribution back to the original coordinate system, we end up with

$$U \begin{pmatrix} \Delta_{lin}(K)\sigma_y & 0 \\ & 0 \\ 0 \quad 0 & 0 \end{pmatrix} U^{-1} = \frac{i\Delta_{lin}(\mathbf{k})}{\sqrt{3}} \begin{pmatrix} 0 & 1 & -1 \\ -1 & 0 & -1 \\ 1 & 1 & 0 \end{pmatrix} . \tag{4.13}$$

This result cannot be used directly to derive the Schwinger-Dyson equation, since we already discussed the problems related to the derivation of the linear Hamiltonian. However, it shows some interesting characteristics that we are willing to preserve in our actual gap function, in particular it is a complex Hermitian matrix. To understand the consequences of this property, we can look at the complete Hamiltonian (4.7). It is worth noticing that each term above the diagonal is related to an equivalent term in the lower-left triangle of the matrix. Together, each of these couples expresses that the hopping between two sublattices is independent on the direction. On the contrary, the complex structure of the gap matrix (4.13) explicitly breaks this symmetry, i.e. for instance $A \to B$ is now different from $B \to A$.

This fundamental characteristic can be effectively described by a dimerization process within the Kagome lattice[6]. The corresponding spinless Hamiltonian can be derived similarly to the non-interacting term, namely we start with

$$H = -\delta t \sum_i \left(a_i^\dagger b_{i+\delta_{12}} - a_i^\dagger b_{i-\delta_{12}} + b_{i+\delta_{12}}^\dagger c_{i+\delta_{13}} - b_{i-\delta_{12}}^\dagger c_{i-\delta_{13}} + c_{i+\delta_{13}}^\dagger a_i - c_{i-\delta_{13}}^\dagger a_i - h.c. \right) . \tag{4.14}$$

Here we used the lattice vectors definition to express the different nearest neighbour indexes, so that the sum reduces to the sublattice A only. The minus sign that appears in all the couples like $(a_i^\dagger b_{i+\delta_{12}} - a_i^\dagger b_{i-\delta_{12}})$ indicates that, for instance, while the hopping from the site $i + \delta_{12}$ to i is favoured, the one from $i - \delta_{12}$ to i results dumped. This condition prevents the site i to become an accumulation points towards which the nearby electrons are attracted. Moreover, also the hermitian conjugate enters with a minus sign in the Hamiltonian. In this way, the dimerization process can take place since it guarantees that the hopping in any opposite direction is equally forced(dumped) if the original orientation results dumped(forced). At this point, we can perform the same Fourier transformation that we used in (4.5), hence the dimerization Hamiltonian becomes[6]

$$H^{dim} = -2\delta t \sum_{\sigma,\mathbf{k}} \bar{\Psi}_\sigma(\mathbf{k}) \begin{pmatrix} 0 & i\sin(\mathbf{k} \cdot \boldsymbol{\delta}_{12}) & i\sin(\mathbf{k} \cdot \boldsymbol{\delta}_{13}) \\ -i\sin(\mathbf{k} \cdot \boldsymbol{\delta}_{12}) & 0 & i\sin(\mathbf{k} \cdot \boldsymbol{\delta}_{23}) \\ -i\sin(\mathbf{k} \cdot \boldsymbol{\delta}_{13}) & -i\sin(\mathbf{k} \cdot \boldsymbol{\delta}_{23}) & 0 \end{pmatrix} \Psi_\sigma(\mathbf{k}) . \tag{4.15}$$

First of all, we see that the complex Hermitian structure of matrix (4.13) is preserved. Furthermore, if we compute the dimerization matrix at the Dirac point $\mathbf{K}_D = \left(\frac{2\pi}{3a}, 0 \right)$, we get

$$h^{dim}(\mathbf{K}_D) = i\sqrt{3}\delta t \begin{pmatrix} 0 & 1 & -1 \\ -1 & 0 & -1 \\ 1 & 1 & 0 \end{pmatrix} ,$$

that looks exactly as (4.13) for a mass gap equal to $\Delta_{lin}(\mathbf{K}_D) = 3\delta t$. At this point we can study how the total Bloch Hamiltonian $h(\mathbf{k}) = h_0(\mathbf{k}) + h^{dim}(\mathbf{k})$ behaves for a non-zero dimerization parameter $\delta t \neq 0$. The new energy bands are

$$\begin{cases} E_{1,2}(\mathbf{k}) = -t\left(1 \pm \sqrt{2\delta t^2 \left(3 - \sum_j \cos(2\mathbf{k} \cdot \boldsymbol{\delta}_j)\right) + t^2 \left(3 + 2\sum_j \cos(2\mathbf{k} \cdot \boldsymbol{\delta}_j)\right)}\right) \\ E_3(\mathbf{k}) = 2t \end{cases}$$

(4.16)

At each Weyl nodes in the first Brillouin zone we have $\sum_j \cos(2\mathbf{K}_D \cdot \boldsymbol{\delta}_j) = -1.5$, thus a finite energy gap equal to $6\delta t$ is opened. Moreover, we see that the flat band is not affected by the dimerization process. This is due in part to the vanishing structure of the Bloch Hamiltonian (4.15) for $\mathbf{k} = 0$. However, we also need to assume that the dimerization happens with the same intensity along each possible direction, i.e. δt does not depend on the sublattices considered. This is not necessary true in general, and we could deal with a vectorial parameter $\boldsymbol{\eta} = (\eta_1, \eta_2, \eta_3)$, where the three components correspond to $\boldsymbol{\delta}_{12}$, $\boldsymbol{\delta}_{13}$ and $\boldsymbol{\delta}_{23}$ respectively. Under this assumption, the middle band would still touch the flat one at $E = 2t$, but away from the origin the flat band would no longer have a constant energy. However, throughout the rest of the thesis we will assume that the dimerization happens symmetrically, i.e. we will ignore its vectorial character.

To sum up, we found that if we introduce a mass function proportional to this dimerization matrix, we will be able to open an energy gap at the Dirac points. In other words, this is the analogue to the symmetry breaking process that leads to the CDW ground state in the case of graphene. In fact, while for graphene we were able to distinguish the two sublattices by the net charge difference, now the time-reversal symmetry gets broken by the internal hopping direction of the dimers. This implies that we can take the order parameter to be the function proportional to the matrix (4.15). In the next sections we will study how this parameter behaves as a function of the coupling parameter $\alpha = e^2/(4\pi\epsilon v_F)$.

4.3 Polarization Function

In order to derive the polarization function, we can start introducing the non-interacting inverse Green's function

$$G_0^{-1}(\mathbf{k}, \omega) = -i\omega \mathbb{1} + h_0(\mathbf{k}) \ , \tag{4.17}$$

where $h_0(\mathbf{k})$ is the Bloch Hamiltonian of the non-interacting system (4.7). Due to the presence of an additional energy band in the Kagome structure, the Green's function is now a 3x3 matrix rather than just 2x2. We can also invert this expression to work out the actual non-interacting Green's function

$$G_0(\mathbf{k}, \omega) = \frac{\mathbf{M}}{(2t - i\omega)\left(\omega^2 - 2it\omega + 2t^2\left(1 + \sum_j \cos(2\mathbf{k} \cdot \boldsymbol{\delta}_j)\right)\right)} \ , \tag{4.18}$$

where $\mathbf{M}$ is a 3x3 matrix that comes from G_0^{-1}. What we want to show here is that the denominator of (4.18) recalls exactly the non-interacting energy structure (4.8), which will be useful to integrate out the frequency using the residue theorem in the complex plane. At this point, we can define the polarization function in complete analogy to what we did for graphene, namely equation (3.19), and the analytical expression becomes

$$
\Pi(\mathbf{k},\omega) = 2 \int \frac{d\nu}{2\pi} \frac{d\mathbf{q}}{(2\pi)^2} \frac{\sum_j \left[(\omega+\nu)^2 - 2t^2 \left(1 + \cos(2(\mathbf{k}+\mathbf{q})\cdot\boldsymbol{\delta}_j)\right)\right] \times}{(2t - i\nu)\left(\nu^2 - 2it\nu + 2t^2\left(1 + \sum_j \cos(2\mathbf{q}\cdot\boldsymbol{\delta}_j)\right)\right)}
$$

$$
\frac{\left[\nu^2 - 2t^2\left(1 + \cos(2\mathbf{q}\cdot\boldsymbol{\delta}_j)\right)\right] + 8t^2 \sum_j \left[\nu^2 \cos(\mathbf{q}\cdot\boldsymbol{\delta}_j) + 2t\cos(\mathbf{q}\cdot\boldsymbol{\delta}_{j+1})\cos(\mathbf{q}\cdot\boldsymbol{\delta}_{j+2})\right] \times}{(2t - i(\omega+\nu))\left((\omega+\nu)^2 - 2it(\omega+\nu) + 2t^2\left(1 + \sum_j \cos(2(\mathbf{k}+\mathbf{q})\cdot\boldsymbol{\delta}_j)\right)\right)}
$$

$$
\frac{\left[(\omega+\nu)^2 \cos((\mathbf{k}+\mathbf{q})\cdot\boldsymbol{\delta}_j) + 2t\cos((\mathbf{k}+\mathbf{q})\cdot\boldsymbol{\delta}_{j+1})\cos((\mathbf{k}+\mathbf{q})\cdot\boldsymbol{\delta}_{j+2})\right]}{} \; .
$$

$$(4.19)$$

Here we are using a cyclic relation for the indices, i.e. $\boldsymbol{\delta}_{12} \to \boldsymbol{\delta}_{13} \to \boldsymbol{\delta}_{23} \to \boldsymbol{\delta}_{12}$. Even though the explicit formula results more complex than equation (3.20), we see that also in this case the entire argument is proportional to $1/t^2$, which becomes $1/t$ once we integrate out the frequency dependence. Thus, it is possible to define the reparametrized polarization function as $\tilde{\Pi}(\mathbf{k}, \omega' = \omega/t) = t\Pi(\mathbf{k},\omega)$, which is independent on the hopping parameter value, i.e. it does not depend on the Fermi velocity. It is possible to compute equation (4.19) numerically, using the on-shell condition to get rid of the frequency dependence. The result for the reparametrized function is shown in Fig. 4.3. We see that the outcome recalls almost identically what we got for the graphene case.

4.4 Schwinger-Dyson Equation

The interacting Green's function can be obtained by summing the dimerization matrix to the non-interacting function (4.17). If we define the gap function $\Delta(\mathbf{k})$ as the measure of the dimerization strength, which is proportional to the energy gap at the Dirac points, we get

$$
G^{-1}(\mathbf{k},\omega) = -i\omega\mathbb{1} - 2\begin{pmatrix} 0 & t\cos(k_{12}) + i\Delta(\mathbf{k})\sin(k_{12}) & t\cos(k_{13}) + i\Delta(\mathbf{k})\sin(k_{13}) \\ 0 & t\cos(k_{23}) + i\Delta(\mathbf{k})\sin(k_{23}) \\ & & 0 \end{pmatrix} \; .
$$

$$(4.20)$$

Here we defined $k_j \doteq \mathbf{k}\cdot\boldsymbol{\delta}_j$, and the lower triangle of the second matrix is understood to be filled so that the matrix is hermitian. In principle this expression could lead to three independent self-consistent equations for the directional components of the dimerization parameter. However, since we assumed the dimerization to be symmetric in the different directions, they all reduce to the same equation. In fact, we can write down the Schwinger-Dyson equation for
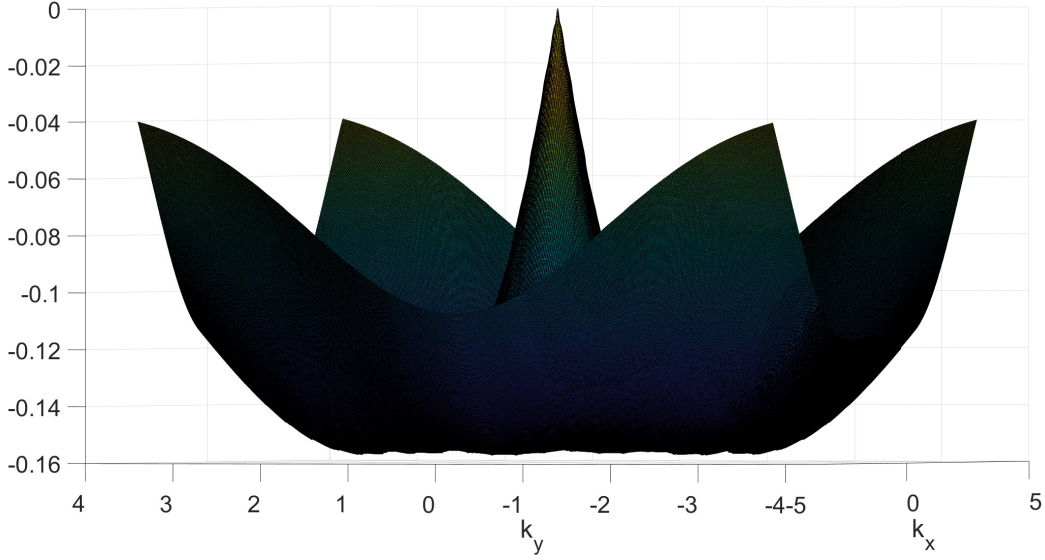
Figure 4.3: Polarization function for the Kagome lattice within the on-shell condition.

each conjugate couple, i.e. for the corresponding lattice direction, as

$$2i\Delta(\mathbf{k})\sin(\mathbf{k}\cdot\boldsymbol{\delta}_j) = \int \frac{d\mathbf{p}}{(2\pi)^2}\frac{d\nu}{2\pi}\,V^{RPA}(\mathbf{k}+\mathbf{p})\,\frac{2i\Delta(\mathbf{p})\sin(\mathbf{p}\cdot\boldsymbol{\delta}_j)(2t-i\nu)}{(\nu_+-\nu)(\nu_--\nu)(2t-i\nu)}\,,\tag{4.21}$$

where the poles $\nu_\pm$ are

$$\nu_\pm = i\left(t\pm\sqrt{2\Delta(\mathbf{p})\left(3-\sum_n\cos(2\mathbf{p}\cdot\boldsymbol{\delta}_n)\right)+t^2\left(3+2\sum_n\cos(2\mathbf{p}\cdot\boldsymbol{\delta}_n)\right)}\right).\tag{4.22}$$

We see from equation (4.21) that the flat band vanishes from the gap equation. This is a direct consequence of the dimerization symmetry, which preserves the flat band entirely. We can now shift the frequency according to the chemical potential t, namely $\nu' \to \nu + it$. In this way the poles become symmetric around the real axis, i.e. $\nu'_\pm = \nu_\pm - it$, and we can integrate the Schwinger-Dyson equation (4.21) using the residue theorem. The self-consistent equation for the gap becomes

$$\Delta(\mathbf{k}) = \int_{BZ}\frac{d\mathbf{p}}{(2\pi)^2}\,V^{RPA}(\mathbf{k}+\mathbf{p})\,\frac{\Delta(\mathbf{p})}{2i\nu'_+\,(\mathbf{p},\Delta(\mathbf{p}))}\,\frac{\sin(\mathbf{p}\cdot\boldsymbol{\delta}_j)}{\sin(\mathbf{k}\cdot\boldsymbol{\delta}_j)}\,.\tag{4.23}$$

It is worth noticing that this expression is actually independent on the specific direction j that we choose. In fact, it is reasonable to assume that the gap function $\Delta(\mathbf{p})$ will be symmetric in all the Dirac points, i.e. symmetric under a rotation of the Brillouin zone of $2\pi/3$ radians. This is because we know that only two of the six Weyl nodes are truly independent, however, we are still free to choose any pair of opposite points. In other words, the invariance under a rotation of $2\pi/3$ radians is necessary to preserve the equivalence between the three possible pairs of independent Dirac points. Moreover, both

the RPA interaction term and the pole function are invariant under the same rotation. Hence, the entire integral results independent on the direction j that we choose, i.e. invariant under a rotation of $2\pi/3$ radians.

It is also worth noticing from equation (4.23) that thanks to the presence of $V^{RPA}(\mathbf{k}+\mathbf{p})$, which diverges at $\mathbf{p} = -\mathbf{k}$, the maximal contribution to the integral is given in the region $\mathbf{p} \simeq -\mathbf{k}$. In those points we have that $\frac{\sin(\mathbf{p}\cdot\boldsymbol{\delta}_j)}{\sin(\mathbf{k}\cdot\boldsymbol{\delta}_j)} \simeq -1$, which gets rid of the minus sign that comes from the complex product $i\nu'_+$. Therefore, when the contribution to the integral is maximum, we recover the same structure of the graphene Schwinger-Dyson equation (3.23).

4.5   Numerical Results

The gap equation (4.23) can now be solved numerically for different values of the coupling parameter α. We use the same technique that we presented for the graphene case, namely we integrate the function using the Gaussian quadrature formula and we find the solution through the iteration algorithm. A representative example of the gap solution profile is shown in Fig. 4.4. We see that it recalls the typical solution of the graphene lattice, according to what we argued in the last section.
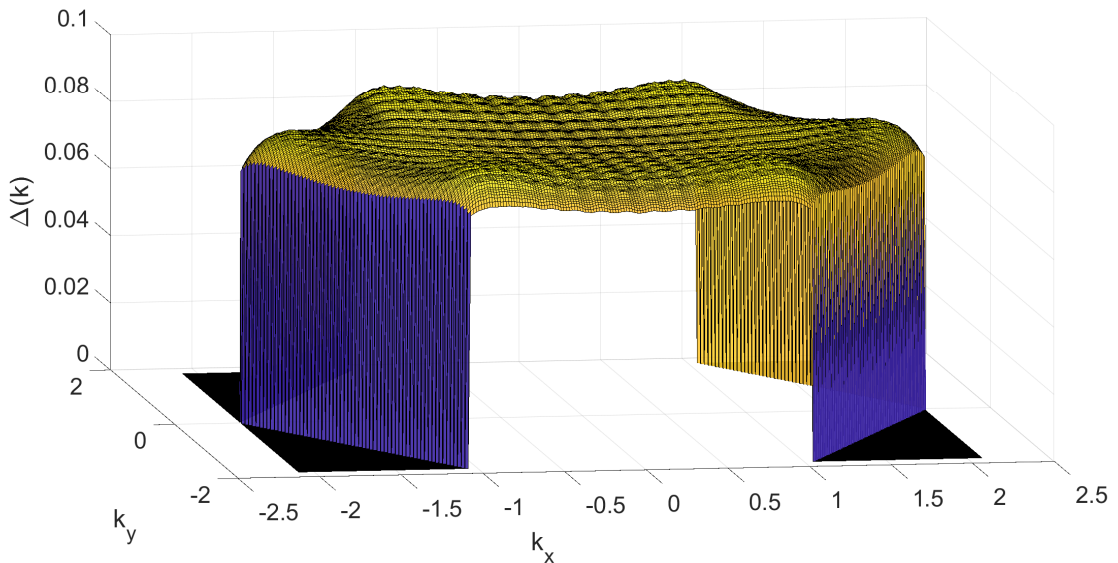

Figure 4.4: Numerical solution of the gap equation with coupling parameter $\alpha = 2.0$.

In order to derive the phase diagram for the Kagome lattice we can look at its energy spectrum (4.16), where now the dimerization parameter δt is substituted by $\Delta(\mathbf{k})$. We see that the actual energy gap at the Dirac point is equal to $6\Delta(\mathbf{K}_D)$, thus we can plot half of this quantity as a function of the coupling parameter in analogy to what we did for graphene. The semimetal-insulator phase diagram is shown in Fig. 4.5.
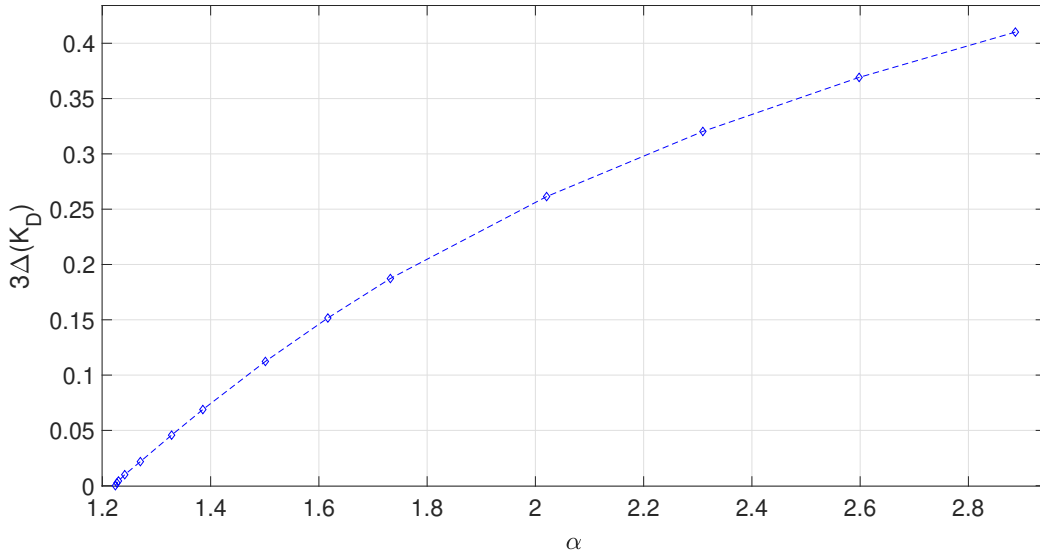
Figure 4.5: Mass gap at the Dirac point as a function of the coupling parameter α.

The critical coupling parameter results $\alpha_c = 1.224$. As we have seen at the beginning of the chapter, a low energy expansion would have lead to the same result of graphene linear theory. Hence, the difference between the Kagome critical coupling parameter and graphene's is partially due to the non-linear part of the models. Moreover, the order parameter is different for the two lattices, which may also play a role in the semimetal-insulator phase transition. In any case, studying the entire Hamiltonian rather than put the focus exclusively on the low energy expansion has allowed us to highlight the differences between the two models. Nevertheless, the two results are similar, which agrees with the hypothesis that the linear contribution is dominant.

Chapter 5

Conclusions

In this thesis we studied the role of the Coulomb interaction in two examples of Weyl semimetal[2]. We first analysed the linear model using the renormalization group theory[9]. This tells us that in the weak coupling limit the interaction contribution becomes irrelevant. However, it is sufficient to draw the analogy with the relativistic QED theory to understand that this is not a sufficient analysis in our case. In fact, we introduce the coupling parameter in our theory as the analogue of the fine-structure constant, namely $\alpha = 1/137$, where now the light speed is substituted by the Fermi velocity of the material. However, we expect this velocity to be roughly of the order of 100 times smaller, which means the coupling parameter would become $\alpha^{material} \sim 100\alpha \sim 1$. This shows that the weak coupling limit is not a good description for the model.

Then, we analysed the graphene lattice in the strong coupling limit[4][13] by studying both its low energy expansion and the whole Hamiltonian. This second approach has allowed us to overcome some internal issues related to the linear expansion of the model. In particular, we get rid of the cut-off momentum Λ, which is not uniquely defined by the theory. We found that in the strong coupling limit an energy gap is opened at the Weyl nodes. Also, we identified the critical coupling parameter below which the material continues to be a gapless semimetal. For the graphene model this parameter is $\alpha_c = 1.333$, thus smaller than the coupling parameter of graphene $\alpha^{graphene} \simeq 2.16$. This suggests that the ground state of the graphene lattice is an insulator rather than a Weyl semimetal, however we also discussed why the experimental evidence of this result is difficult to observe. Finally, we gave an interpretation of the mass function, i.e. of the symmetry breaking process that leads to the semimetal-insulator phase transition. In the case of graphene, this order parameter measures the charge imbalance between the two sublattices that composes the material[17].

In the last part of the thesis we analysed the Kagome lattice[5]. We saw that the low energy expansion of the Hamiltonian leads to the same result of the graphene linear theory. We thus used the complete Hamiltonian approach to include automatically all the corrections due to the non-linear contributions and, in particular, of the additional flat band. The phase diagram resulted similar to the one from the graphene lattice, with $\alpha_c = 1.224$. In this case

the symmetry breaking process related to the phase transition is due to the dimerization that occurs between the three triangular sublattices[6].

In the introduction we saw that a new material has been proposed to be a valid alternative to graphene for the realisation of a strongly correlated viscous electron fluid[8]. In particular, this material posses a Kagome lattice and its coupling parameter is roughly three times larger than the graphene one. Hence, we can conclude that a transition to the insulating phase will probably take place naturally. Consequently, this novel material is not a good candidate to study the hydrodynamic regime in two dimensional Weyl semimetals.

Appendix A

First Order Renormalization Group

In chapter 2 we presented the most significant outcomes from the RG analysis applied to the 2 dimensional linear theory. In this appendix, we will explicitly derive the majority of those results and discuss some of the technical details. For a complete review of the problem we invite you to read the works of Shankar[9].

In equation (2.15) we defined the slow modes, effective action by means of the fast modes average, which can be written as

$$
\langle S_{int} \rangle_> \doteq \frac{\int d\left[\bar{\Psi}_>\right] d\left[\Psi_>\right] e^{-S_0\left[\bar{\Psi}_>, \Psi_>\right]} S_{int}\left[\bar{\Psi}_>, \ \Psi_>, \ \bar{\Psi}_<, \ \Psi_<\right]}{\int d\left[\bar{\Psi}_>\right] d\left[\Psi_>\right] e^{-S_0\left[\bar{\Psi}_>, \Psi_>\right]}}
$$

$$
= \frac{1}{Z_0^>} \int d\left[\bar{\Psi}_>\right] d\left[\Psi_>\right] e^{-S_0\left[\bar{\Psi}_>, \Psi_>\right]} S_{int}\left[\bar{\Psi}_>, \ \Psi_>, \ \bar{\Psi}_<, \ \Psi_<\right] \ ,
$$

where the definition of the free partition function $Z_0^>$ is implicit. From this expression we can derive all the possible terms that contribute to the effective action. Hence, recalling that the interacting action defined by equation (2.9) is quartic in the fields, there are only three non-vanishing contributions, namely

$$
\left\langle S_{int}\left[\bar{\Psi}_>, \ \Psi_>, \ \bar{\Psi}_<, \ \Psi_<\right]\right\rangle_> = \left\langle S_{int}\left[\bar{\Psi}_>, \ \Psi_>\right]\right\rangle_{>,0} + \left\langle S_{int}\left[\bar{\Psi}_<, \ \Psi_<\right]\right\rangle_{>,1}
$$

$$
+ \left\langle S_{int}\left[\bar{\Psi}_>, \ \Psi_>, \ \bar{\Psi}_<, \ \Psi_<\right]\right\rangle_{>,2} \ .
$$

(A.1)

The first term, where all the fields present their short wavelength component only, there is not dependence on the slow modes. This means that the average integral produces a constant contribution, thus irrelevant to the RG analysis. The second term coincides with equation (2.9) for the slow modes only, in fact

$$
\left\langle S_{int}\left[\bar{\Psi}_<, \ \Psi_<\right]\right\rangle_{>,1} = \frac{1}{Z_0^>} \int d\left[\bar{\Psi}_>\right] d\left[\Psi_>\right] e^{-S_0\left[\bar{\Psi}_>, \Psi_>\right]} S_{int}\left[\bar{\Psi}_<, \ \Psi_<\right]
$$

$$
= S_{int}\left[\bar{\Psi}_<, \ \Psi_<\right]
$$

(A.2)

Finally, the last term is non-zero only if both the creation and the annihilation operators have one slow and one fast modes component. Thus, recalling equation (2.9), we can write it in its generic form

$$
\langle S_{int}\rangle_{>,2} = 2\prod_{n=1}^{4}\int_{-\infty}^{\infty}\frac{d\omega_n}{2\pi}\int_{\Lambda/b}^{\Lambda}\frac{d\mathbf{p}_1}{(2\pi)^2}\frac{d\mathbf{p}_3}{(2\pi)^2}\int_{0}^{\Lambda/b}\frac{d\mathbf{p}_2}{(2\pi)^2}\frac{d\mathbf{p}_4}{(2\pi)^2}\int_{|\mathbf{q}|=0}^{\Lambda}\frac{d\mathbf{q}}{(2\pi)^2}\frac{2\pi e^2}{4\pi\epsilon}\frac{1}{|\mathbf{q}|}
$$

$$
\bar{\Psi}_{<}(\mathbf{p}_2,\omega_2)\;(2\pi)^3\,\delta\left(\mathbf{p}_3-\mathbf{p}_1\right)\delta\left(\omega_3-\omega_1\right)G_{0,>}\left(\mathbf{p}_3,\omega_3\right)\;\Psi_{<}(\mathbf{p}_4,\omega_4)
$$

$$
(2\pi)^2\,\delta\left(\mathbf{p}_1-\mathbf{p}_4-\mathbf{q}\right)(2\pi)^2\,\delta\left(\mathbf{p}_2-\mathbf{p}_3+\mathbf{q}\right)(2\pi)\,\delta\left(\omega_1+\omega_2-\omega_3-\omega_4\right)\;.
$$

$$(A.3)$$

The factor 2 in front of the expression counts the symmetry between the two electrons involved in the process (see Fig. 2.3). The Green's function has been introduced using its canonical definition, namely

$$
\frac{1}{Z_0^{>}}\int d\left[\bar{\Psi}_{>}\right]d\left[\Psi_{>}\right]e^{-S_0\left[\bar{\Psi}_{>},\Psi_{>}\right]}\bar{\Psi}_{>}\left(\mathbf{p}_1,\omega_1\right)\Psi_{>}\left(\mathbf{p}_3,\omega_3\right)=\left\langle\bar{\Psi}_{>}\left(\mathbf{p}_1,\omega_1\right)\Psi_{>}\left(\mathbf{p}_3,\omega_3\right)\right\rangle_{>}
$$

$$
\doteq G_{0,>}\left(\mathbf{p}_1,\mathbf{p}_3,\omega_1,\omega_3\right)
$$

$$
= (2\pi)^3\,\delta\left(\mathbf{p}_3-\mathbf{p}_1\right)\delta\left(\omega_3-\omega_1\right)G_{0,>}\left(\mathbf{p}_3,\omega_3\right)\;.
$$

$$(A.4)$$

It is worth noticing that the last equation in (A.4) is in particular true for translationally invariant system, like the one in exam, but it does not hold in general. The expression in (A.3) can be developed by integrating out the redundant dependencies, i.e.

$$
\langle S_{int}\rangle_{>,2} = 2\prod_{n=2}^{4}\int_{-\infty}^{\infty}\frac{d\omega_n}{2\pi}\int_{\Lambda/b}^{\Lambda}\frac{d\mathbf{p}_3}{(2\pi)^2}\int_{0}^{\Lambda/b}\frac{d\mathbf{p}_2}{(2\pi)^2}\frac{d\mathbf{p}_4}{(2\pi)^2}\int_{|\mathbf{q}|=0}^{\Lambda}\frac{d\mathbf{q}}{(2\pi)^2}\frac{2\pi e^2}{4\pi\epsilon}\frac{1}{|\mathbf{q}|}
$$

$$
\bar{\Psi}_{<}(\mathbf{p}_2,\omega_2)\;G_{0,>}\left(\mathbf{p}_3,\omega_3\right)\;\Psi_{<}(\mathbf{p}_4,\omega_4)\,(2\pi)^2\,\delta\left(\mathbf{p}_3-\mathbf{p}_4-\mathbf{q}\right)
$$

$$
(2\pi)^2\,\delta\left(\mathbf{p}_2-\mathbf{p}_3+\mathbf{q}\right)(2\pi)\,\delta\left(\omega_2-\omega_4\right)
$$

$$
= 2\prod_{n=3}^{4}\int_{-\infty}^{\infty}\frac{d\omega_n}{2\pi}\int_{\Lambda/b}^{\Lambda}\frac{d\mathbf{p}_3}{(2\pi)^2}\int_{0}^{\Lambda/b}\frac{d\mathbf{p}_4}{(2\pi)^2}\int_{|\mathbf{q}|=0}^{\Lambda}\frac{d\mathbf{q}}{(2\pi)^2}\frac{2\pi e^2}{4\pi\epsilon}\frac{1}{|\mathbf{q}|}
$$

$$
\bar{\Psi}_{<}(\mathbf{p}_3-\mathbf{q},\omega_4)\;G_{0,>}\left(\mathbf{p}_3,\omega_3\right)\;\Psi_{<}(\mathbf{p}_4,\omega_4)\,(2\pi)^2\,\delta\left(\mathbf{p}_3-\mathbf{p}_4-\mathbf{q}\right)
$$

$$
= 2\prod_{n=3}^{4}\int_{-\infty}^{\infty}\frac{d\omega_n}{2\pi}\int_{\Lambda/b}^{\Lambda}\frac{d\mathbf{p}_3}{(2\pi)^2}\int_{0}^{\Lambda/b}\frac{d\mathbf{p}_4}{(2\pi)^2}\frac{2\pi e^2}{4\pi\epsilon}\frac{1}{|\mathbf{p}_3-\mathbf{p}_4|}\bar{\Psi}_{<}\left(\mathbf{p}_4,\omega_4\right)
$$

$$
G_{0,>}\left(\mathbf{p}_3,\omega_3\right)\;\Psi_{<}(\mathbf{p}_4,\omega_4)
$$

$$
= 2\frac{2\pi e^2}{4\pi\epsilon}\int_{-\infty}^{\infty}\frac{d\omega_4}{2\pi}\int_{0}^{\Lambda/b}\frac{d\mathbf{p}_4}{(2\pi)^2}\bar{\Psi}_{<}\left(\mathbf{p}_4,\omega_4\right)\Sigma^{(1)}\left(\mathbf{p}_4\right)\Psi_{<}\left(\mathbf{p}_4,\omega_4\right)\;,
$$

$$(A.5)$$

where, in the last equation, we implicitly defined

$$\Sigma^{(1)}\left(\mathbf{p}_4\right) = \int_{-\infty}^{\infty} \frac{d\omega_3}{2\pi} \int_{\Lambda/b}^{\Lambda} \frac{d\mathbf{p}_3}{(2\pi)^2} \frac{1}{|\mathbf{p}_3 - \mathbf{p}_4|} G_{0,>}\left(\mathbf{p}_3, \omega_3\right) \ . \qquad (A.6)$$

This function represents the usual self energy due to the one-loop correction (see Fig. 2.4). It is worth noticing that here we are considering the low-momenta regime, i.e. the long wavelength limit. In other words, this means the significant corrections due to the electron-electron Coulomb interactions are those in the long range limit, which are usually screened. This is due to the vanishing density of states that we observe in the vicinity of the Dirac points.

Appendix B

Numerical Methods

In this appendix we will present some of the numerical techniques that we used throughout the entire project. In particular, we will justify the recursive algorithm employed to solve the Schwinger-Dyson equation, and describe the Gaussian integration formula.

B.1 Recursive Algorithm

Each of the Schwinger-Dyson equations derived in the previous chapters can be seen as integral equations for the gap function $\Delta(\mathbf{k})$. Often, these type of expressions do not have an analytical solution, consequently, finding an efficient method to solve them can be fundamental. In our case, it was worth noticing that the numerical solutions produced by initial guesses had two significant properties: they varied slowly both over the whole domain and between consecutive steps. Moreover, the closer the numerical solution is to the exact mass function, the slower it transforms at each step.

Combining all these properties together, we can assume that if the (n-1)-th recursive step lies completely above or below the actual non-trivial solution, so it will its integral result, i.e. $\Delta_n(\mathbf{k})$. In fact, we can see the evolution of the recursive algorithm as a classic double-well potential problem. If the coupling parameter is larger than its critical value, the Schwinger-Dyson equation admits both the trivial and a non-trivial solution, which play the role of local minima for the algorithm. The error function, defined as the relative difference between two consecutive solutions (eq. B.1), can be thought as a measure of this potential. Hence, observing that the recursive steps evolve monotonously and slowly, we conclude that the non-trivial solutions can be approached from opposite sides, i.e. according to the relation (3.15).

With this method we find two distinct solutions for each value of the coupling parameter. Consequently, we are able to evaluate the error associated to each numerical result given that we assumed the actual solution lies between these two. This is an important consequence of the recursive method since the error function used to run the algorithm is not directly associated to the

solution error. In particular, the error function is defined as

$$f_n \doteq \sum_i \frac{\left|\Delta_n(\mathbf{k}_i) - \Delta_{n-1}(\mathbf{k}_i)\right|}{\left|\Delta_n(\mathbf{k}_i) + \Delta_{n-1}(\mathbf{k}_i)\right|} \ , \tag{B.1}$$

where the sum is taken over the grid that covers the first Brillouin zone. Thus, we stop the recursion when the condition $f_n < \epsilon$ is satisfied for an arbitrary ϵ fixed a priori. However, choosing the same ϵ for each value of the coupling parameter does not guarantee that the error associated to the actual solution will be fixed. In particular, we observed that approaching the critical coupling, both the number of steps required to satisfy the aforementioned condition and the total error, i.e. the difference between the two numerical solutions, increase rapidly (see Fig. B.1 and B.2).
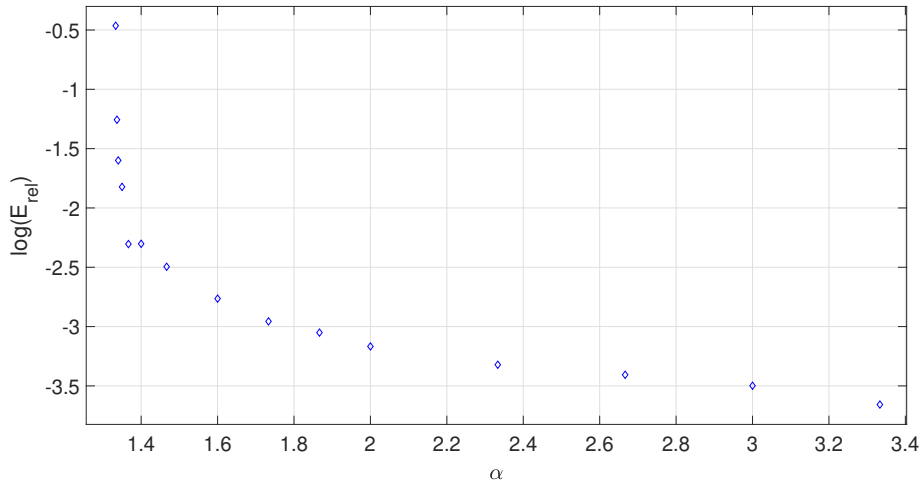

Figure B.1: Relative error defined by (B.1) for each numerical solution of the graphene model.
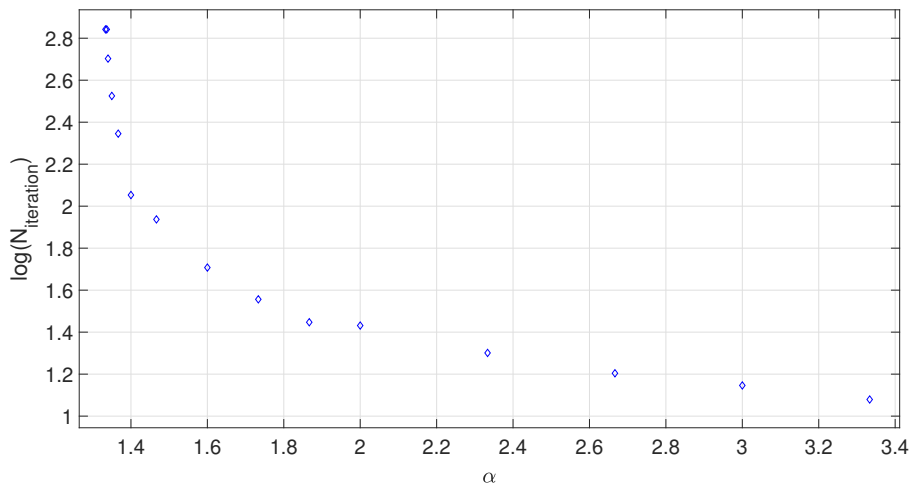

Figure B.2: Number of iteration steps as a function of the coupling parameter α for the graphene model.

B.2 Gaussian Quadrature

We argued that the recursive algorithm is an effective method to solve the integral gap equations that we found in the previous chapters. However, each step of this algorithm requires that we compute a two-dimensional integral over a grid that contains enough points to cover the first Brillouin zone effectively. In other words, if the mass function is sampled over an $M \times M$ grid, each step corresponds to compute M^2 integrals over the Brillouin zone. An effective method to deal with such a high volume of integrals is given by the Gaussian quadrature formula[24][25], which is able to reduce the integration to a very limited number of points.

Every numerical integration method comes down to choose the appropriate grid $\{x_i\}$ and the corresponding weights $\{w_i\}$ for the general formula

$$\int_a^b f(x)dx = \sum_{i=0}^{N-1} w_i f(x_i) \ . \tag{B.2}$$

It is worth noticing that a Taylor expansion based integration formula over N points would be able to integrate exactly a polynomial of degree $(N-1)$. The core idea of the Gaussian quadrature formula is to improve this method by choosing the weights by means of N orthogonal polynomials. In this way we add N further constrains to the formula, that means we can integrate exactly a polynomial of order $(2N-1)$ using only N integration points. We can think of the quadrature formulas as a sequence determined by its N-th element

$$Q_N(f) = \sum_{i=0}^{N-1} w_i^{(N)} f\left(x_i^{(N)}\right) \ , \tag{B.3}$$

which converges if

$$Q_N(f) \xrightarrow[N \to \infty]{} Q(f) = \int_a^b f(x)dx \ . \tag{B.4}$$

The next step is to find the correct grid and weights such that the following integral

$$\int P_{2N-1}(x)dx = \sum_{i=0}^{N-1} w_i P_{2N-1}(x_i)$$

results exact for a generic $(2N-1)$-th order polynomial.

In the standard Gaussian quadrature this is done by using the Legendre polynomials. They are defined by the recursive formula

$$L_{n+1}(x) = \frac{1}{n+1}\left((2n+1)\, x L_n(x) - n L_{n-1}(x) \right) \ , \tag{B.5}$$

where we also have

$$L_0(x) = 1 \quad \text{and} \quad L_1(x) = x \ .$$

Furthermore, the N-th order Legendre polynomial has exactly N zeros in the open interval $(-1, 1)$, and they satisfy the following orthogonality relation

$$\int_{-1}^{1} L_i(x) L_j(x) dx = \frac{2}{2i+1} \delta_{ij} . \tag{B.6}$$

At this point, we notice that a $(2N-1)$-th order polynomial can be written generally as

$$P_{2N-1}(x) = L_N(x) P_{N-1}(x) + Q_{N-1}(x) ,$$

where $L_N(x)$ is the Legendre polynomial defined above, while $P_{N-1}(x)$ and $Q_{N-1}(x)$ are any two polynomial of order $(N-1)$. Hence, if we approximate the integrated function with this polynomial, we get

$$\int_{-1}^{1} f(x) dx \simeq \int_{-1}^{1} P_{2N-1}(x) dx$$

$$= \int_{-1}^{1} \Big(L_N(x) P_{N-1}(x) + Q_{N-1}(x) \Big) dx \tag{B.7}$$

$$= \int_{-1}^{1} Q_{N-1}(x) dx ,$$

where we used the Legendre orthogonality (B.6) to obtain the final expression. The survived function can be defined by means of the Legendre zeros, i.e. given $\{x_k\}_{(k=0,\dots,N-1)}$ such that $L_N(x_k) = 0$, we get $P_{2N-1}(x_k) = Q_{N-1}(x_k)$. Thus, since the polynomial $Q_{N-1}(x)$ is of order $(N-1)$, it results completely determined by its value in N distinct points. However, this function can also be expressed in terms of the Legendre polynomials

$$Q_{N-1}(x) = \sum_{i=0}^{N-1} \alpha_i L_i(x)$$

by choosing the correct factors α's. Hence, knowing that $L_0(x) = 1$ and using the orthogonality (B.6), we can write

$$\int_{-1}^{1} Q_{N-1}(x) = \sum_{i=0}^{N-1} \alpha_i \int_{-1}^{1} L_0(x) L_i(x) dx = 2\alpha_0 . \tag{B.8}$$

Finally, we define the Legendre matrix by

$$Q_{N-1}(x_k) = \sum_{i=0}^{N-1} \alpha_i L_i(x_k) = \sum_{i=0}^{N-1} \alpha_i L_{ik} ,$$

where x_k are the zeros of the N-th order Legendre polynomial. Since the Legendre polynomials are linearly independent, because they are orthogonal, we can invert the matrix to get

$$\sum_{i=0}^{N-1} \left(L^{-1} \right)_{ki} Q_{N-1}(x_i) = \alpha_k .$$

In particular, we can work out the first coefficient α_0 as

$$\begin{aligned}
\alpha_0 &= \sum_{i=0}^{N-1} \left(L^{-1}\right)_{0i} Q_{N-1}(x_i) \\
&= \sum_{i=0}^{N-1} \left(L^{-1}\right)_{0i} P_{2N-1}(x_i) \ .
\end{aligned} \tag{B.9}$$

Hence, combining this result with equations (B.7) and (B.8), we obtain the Gaussian quadrature formula[24]

$$\int_{-1}^{1} f(x)dx \simeq \sum_{i=0}^{N-1} 2 \left(L^{-1}\right)_{0i} P_{2N-1}(x_i) \ . \tag{B.10}$$

This is an integration formula with weights $w_i = 2 \left(L^{-1}\right)_{0i}$, and the grid is defined by the N zeros in the interval $(-1, 1)$ of the N-th order Legendre polynomial. It is worth to emphasise that this is an exact method to integrate a $(2N - 1)$-th order polynomial, thus the only approximation we are doing in the equation (B.9) is due to $f(x) \simeq P_{2N-1}(x)$. In order to use this integration method, we can determine the Legendre polynomials by means of the recursive formula (B.5), and find their zeros using a combination of the bisection method and the Newton-Raphson algorithm.

Bibliography

[1] K. S. Novoselov. Electric field effect in atomically thin carbon films. *Science*, 306(5696):666–669, Oct 2004.

[2] Sumathi Rao. Weyl semi-metals : a short review, 2016.

[3] A. H. Castro Neto, F. Guinea, N. M. R. Peres, K. S. Novoselov, and A. K. Geim. The electronic properties of graphene. *Reviews of Modern Physics*, 81(1):109–162, Jan 2009.

[4] Valeri N. Kotov, Bruno Uchoa, Vitor M. Pereira, F. Guinea, and A. H. Castro Neto. Electron-electron interactions in graphene: Current status and perspectives. *Reviews of Modern Physics*, 84(3):1067–1125, Jul 2012.

[5] C Barreteau, F Ducastelle, and T Mallah. A bird's eye view on the flat and conic band world of the honeycomb and kagome lattices: towards an understanding of 2d metal-organic frameworks electronic structure. *Journal of Physics: Condensed Matter*, 29(46):465302, Oct 2017.

[6] H.-M. Guo and M. Franz. Topological insulator on the kagome lattice. *Physical Review B*, 80(11), Sep 2009.

[7] Marco Polini and Andre K. Geim. Viscous electron fluids. *Physics Today*, 73(6):28–34, Jun 2020.

[8] Domenico Di Sante, Johanna Erdmenger, Martin Greiter, Ioannis Matthaiakakis, René Meyer, David Rodríguez Fernández, Ronny Thomale, Erik van Loon, and Tim Wehling. Turbulent hydrodynamics in strongly correlated kagome metals. *Nature Communications*, 11(1), Aug 2020.

[9] R. Shankar. Renormalization-group approach to interacting fermions. *Reviews of Modern Physics*, 66(1):129–192, Jan 1994.

[10] H.T.C. Stoof, D.B.EM. Dickerscheid, and K. Gubbels. Ultracold quantum fields. 2009.

[11] A. Atland and B.D. Simons. Condensed matter field theory. 2010.

[12] E. H. Hwang and S. Das Sarma. Dielectric function, screening, and plasmons in two-dimensional graphene. *Phys. Rev. B*, 75:205418, May 2007.

[13] D.V. Khveshchenko and H. Leal. Excitonic instability in layered degenerate semimetals. *Nuclear Physics B*, 687(3):323–331, May 2004.

[14] O. V. Gamayun, E. V. Gorbar, and V. P. Gusynin. Gap generation and semimetal-insulator phase transition in graphene. *Physical Review B*, 81(7), Feb 2010.

[15] M. Q. Huber. Derivation of dyson-schwinger equations. 2017.

[16] Gordon W Semenoff. Chiral symmetry breaking in graphene. *Physica Scripta*, T146:014016, Jan 2012.

[17] C. L. Kane and E. J. Mele. Quantum spin hall effect in graphene. *Physical Review Letters*, 95(22), Nov 2005.

[18] D. V. Khveshchenko. Magnetic-field-induced insulating behavior in highly oriented pyrolitic graphite. *Physical Review Letters*, 87(20), Oct 2001.

[19] Anand Sharma, Valeri N. Kotov, and Antonio H. Castro Neto. Excitonic mass gap in uniaxially strained graphene. *Physical Review B*, 95(23), Jun 2017.

[20] D V Khveshchenko. Massive dirac fermions in single-layer graphene. *Journal of Physics: Condensed Matter*, 21(7):075303, Jan 2009.

[21] Linda Ye, Mingu Kang, Junwei Liu, Felix von Cube, Christina R. Wicker, Takehito Suzuki, Chris Jozwiak, Aaron Bostwick, Eli Rotenberg, David C. Bell, and et al. Massive dirac fermions in a ferromagnetic kagome metal. *Nature*, 555(7698):638–642, Mar 2018.

[22] I. I. Mazin, Harald O. Jeschke, Frank Lechermann, Hunpyo Lee, Mario Fink, Ronny Thomale, and Roser Valentí. Theoretical prediction of a strongly correlated dirac metal. *Nature Communications*, 5(1), Jul 2014.

[23] S. A. Owerre, A. A. Burkov, and Roger G. Melko. Linear spin-wave study of a quantum kagome ice. *Phys. Rev. B*, 93:144402, Apr 2016.

[24] Morten Hjorth-Jensen. Computational physics. Fall 2010.

[25] S. E. Mousavi, H. Xiao, and N. Sukumar. Generalized gaussian quadrature rules on arbitrary polygons. *International Journal for Numerical Methods in Engineering*, 82(1):99–113, 2010.